

PFC/RR-81-21

PLASMA POSITION CONTROL ON ALCATOR C

Patrick A. Pribyl

Plasma Fusion Center
Massachusetts Institute of Technology
Cambridge, MA 02139

May, 1981

This work was supported by the U.S. Department of Energy Contract No. DE-AC02-78ET51013. Reproduction, translation, publication, use and disposal, in whole or in part, by or for the United States government is permitted.

PLASMA POSITION CONTROL ON ALCATOR C

by

Patrick A. Pribyl

ABSTRACT

The Alcator C MHD equilibrium is investigated from the standpoint of determining the plasma position. A review of equilibrium theory is presented, indicating that the central flux surfaces of the plasma should be displaced about 1-2 cm from the outermost. Further, the plasma should have a slightly noncircular cross-section. A comparison is made between the observed and predicted profiles. Flux loops sensitive to plasma position generate the error signal for the feedback control circuit. This measurement agrees with other position-sensitive diagnostics, such as limiter heating, and centroids of density, soft X-ray, and electron cyclotron emission. A linear model is developed for the position control feedback system, including the vertical field SCR supply, plasma, and feedback electronics. Operation of the control system agrees well with that predicted by the model, with acceptable plasma position being maintained for the duration of the discharge. The feedback control system is in daily use for Alcator C runs.

Supervised by R. Parker, Professor of Electrical Engineering

Table of Contents

	<u>Page</u>
1. INTRODUCTION	8
2. THEORY	10
2.1 Magnetohydrodynamic Description of the Plasma	10
2.2 Solutions to the Grad-Shafranov Equation	12
2.2.1 One-Dimensional Pressure Balance (Zero-Order)	14
2.2.2 "Shafranov Shift" and Non-circularity (First Order)	15
2.2.2.1 "Shafranov Shift"	15
2.2.2.2 Non-circularity	22
2.3 The Vertical Field Required for Equilibrium	31
3. THE FEEDBACK SYSTEM	33
3.1 A Model of the Feedback Loop	36
3.1.1 The Vertical Field Power Supply	38
3.1.2 The Plasma and Position Sensing Response	43
3.1.3 The Feedback Circuit	45
3.1.4 Stability and Response of the Feedback System	46
3.2 The Position Sensing Pickup Coils	52
3.3 The Vertical Field	57
3.3.1 The Vacuum Vertical Field	57
3.3.2 Time Delays Associated with the Vertical Field	60
3.4 Stray Fields Affecting the Plasma	61

Table of Contents, Continued

	<u>Page</u>
4. PERFORMANCE AND RESULTS	64
4.1 Performance	64
4.2 Results	73
5. CONCLUSIONS	80
APPENDIXES	
I. A Derivation of the Grad Shafranov Equation	82
II. Delays Due to the Vertical Field Penetration of the Tokamak Structure	87
A.II.1 Penetration of the Vertical Field through the Toroidal Field Magnet	87
A.II.1.1 Case 1	87
A.II.1.2 Case 2	90
A.II.2 Penetration through the Vacuum Chamber Wall	92
A.II.3 Machine Penetration-Time Measurements	93
III. Magnetic Field Strengths in Alcator C	97
A.III.1 Midplane Values of the Fields and their Indexes	97
A.III.2 Fourier Harmonics in Fields Present in Alcator C	103
IV. The Feedback Circuit--Description and Schematic	104
A.IV.1 The Integrators	104
A.IV.2 The Rest of the Circuit	108
ACKNOWLEDGEMENTS	110
REFERENCES	111

List of Figures

<u>Number</u>	<u>Title</u>	<u>Page</u>
2.1	Comparison of empirical temperature and density profiles (crosses) with those used in the flux surface calculation.	19
2.2	The poloidal beta and internal inductance, as functions of radius.	20
2.3	The plasma flux surfaces.	21
2.4	Graphs of the first order homogeneous solution of the Grad-Shafranov equation.	23
2.5	Harmonically perturbed flux surfaces.	25
2.6	Interferometer density data (+'s) compared with the theoretical line integral of the density.	27
3.1	The feedback system.	34
3.2	A linear model of the feedback loop, used in the stability analysis.	37
3.3	A linear model of the vertical field SCR supply.	39
3.4	Bode plots of the closed loop response of the vertical field power supply (as modelled).	42
3.5	Bode plots of the feedback system open loop transmission (as modelled).	
	a) The case of no frequency compensation from the feedback circuit results in unstable closed loop response.	47
	b) The normal operating settings are used to generate the response plot.	48
3.6	Bode plots of the closed loop frequency response of the feedback system.	
	a) The excitation is a programming signal, while the response is the position signal V_{C-S} .	50
	b) The excitation is an equivalent plasma disturbance, while the response is the position signal	51
3.7	The position sensing pickup coils.	53
3.8	The vacuum vertical field.	58

List of Figures, Continued

<u>Number</u>	<u>Title</u>	<u>Page</u>
3.9	The stray component of the toroidal field, as nulled by the bias field. a) the stray toroidal field. b) the bias field. c) their sum.	62
4.1	A typical Alcator C plasma discharge.	65
4.2	The plasma response to a programmed step in position.	67
4.3	Plasma disruptions. a) Minor disruption of the plasma. b) A somewhat larger disruption.	68 69
4.4	Unstable operation of the feedback system (no lead).	71
4.5	Unstable operation of the feedback system (too much gain).	72
4.6	Comparison of position-sensitive diagnostics with the flux surface measurement.	74
4.7	Positions measured by electron cyclotron emission, plotted against measured flux surface position.	76
4.8	Differential limiter heating vs. average position of the outer flux surface.	78
A.I.1	The toroidal coordinate system.	86
A.II.1	The toroidal field Bitter plate construction.	88
A.II.2	Field penetration, case 1. A vertical field is applied perpendicular to the ends of infinitely wide plates.	89
A.II.3	Field penetration case 2. A vertical field is applied parallel to the sides of infinitely long plates.	91
A.II.4	Detected radial and poloidal field at the vacuum chamber surface for an applied horizontal field.	94

List of Figures, Continued

<u>Number</u>	<u>Title</u>	<u>Page</u>
A.II.5	Detected radial and poloidal fields at the vacuum chamber surface for an applied vertical field.	95
A.IV.1	The Integrator Circuit.	105
A.IV.2	The Summing and Lead Network.	109

List of Tables

<u>Number</u>	<u>Title</u>	<u>Page</u>
2.1	Plasma Shape Perturbations from Circular, for Various Plasma Conditions.	28
2.1a	The Toroidal Field Single Turn Current is Antiparallel to the Plasma Current.	29
2.1b	The Toroidal Field Single Turn Current is Parallel to the Plasma Current.	30
A.III.1	Midplane Values of the Fields and their Indexes.	97
A.III.1a	EF1 Vertical Field at Midplane, for 1 kA.	97
A.III.1b	EF2 Vertical Field at Midplane, for 1 kA.	98
A.III.1c	DF1 Bias Field at Midplane, for 1 kA.	99
A.III.1d	DF2 Bias Field at Midplane, for 1 kA.	100
A.III.1e	Horizontal Bias Field at Midplane, for 1 kA.	101
A.III.1f	Stray Toroidal Field at Midplane, for 100 kA.	102
A.III.2	Fourier Harmonics in Fields Present in Alcator C.	103
A.III.2a	The Vertical Field Coils, and Vertical Bias Field.	103
A.III.2b	The Horizontal Bias Field.	103
A.III.2c	The Stray Toroidal field.	103

Chapter 1. Introduction

The Alcator C Tokamak is designed to operate with near fusion-grade plasmas. In typical operation, the input power to the plasma is from 1 to 5 MW, resulting in average energy flux at the surface of 20 to 100 W per cm^2 . Local "hot spots" receive much greater energy concentrations. For protection of the interior of the vacuum chamber, and for minimum impurity influx from the walls, it is necessary to accurately control and maintain the plasma position. This is the object of the work presented in this thesis.

The classical method of horizontal plasma position control is to use a vertical magnetic field to act on the plasma current to create a transverse force. Most tokamaks have some sort of position feedback involving perturbations to a pre-programmed field. In addition, many also employ a copper shell around the plasma to compensate for any rapid changes in position, by means of flux conservation forces.

The feedback scheme developed for Alcator C dynamically controls the entire equilibrium vertical field for the plasma. The response of the feedback loop is found to be adequate to maintain the position, even with no copper shell. In this system, a first approximation to the required equilibrium field is derived from the plasma current, with measured position fluctuations forming the feedback error signal.

Theory pertinent to the plasma position equilibrium is presented in Chapter 2. The innermost flux surfaces should

Chapter 1. Introduction

The Alcator C Tokamak is designed to operate with near fusion-grade plasmas. In typical operation, the input power to the plasma is from 1 to 5 MW, resulting in average energy flux at the surface of 20 to 100 W per cm². Local "hot spots" receive much greater energy concentrations. For protection of the interior of the vacuum chamber, and for minimum impurity influx from the walls, it is necessary to accurately control and maintain the plasma position. This is the object of the work presented in this thesis.

The classical method of horizontal plasma position control is to use a vertical magnetic field to act on the plasma current to create a transverse force. Most tokamaks have some sort of position feedback involving perturbations to a pre-programmed field. In addition, many also employ a copper shell around the plasma to compensate for any rapid changes in position, by means of flux conservation forces.

The feedback scheme developed for Alcator C dynamically controls the entire equilibrium vertical field for the plasma. The response of the feedback loop is found to be adequate to maintain the position, even with no copper shell. In this system, a first approximation to the required equilibrium field is derived from the plasma current, with measured position fluctuations forming the feedback error signal.

Theory pertinent to the plasma position equilibrium is presented in Chapter 2. The innermost flux surfaces should

be offset from the center of the plasma cross section, and the outer plasma boundary is theoretically noncircular. These effects are derived by direct integration of the Grad-Shafranov equation [1], and must be taken into account when comparing measurements of the outermost flux surfaces to data from other position sensitive diagnostics (such as centroids of the soft X-ray and density profiles). The feedback system is described in Chapter 3. A linearized model of the system is examined with regards to stability and response. Stray magnetic fields present in the toroidal vessel may affect the plasma equilibrium, and these are discussed in this chapter as well. The feedback system is now employed during normal operation of the Alcator C Tokamak, and results of its use are presented in Chapter 4. Various diagnostics are used to determine the plasma position, including density, soft X-ray and electron cyclotron emission profiles, and limiter thermocouples, and this information is compared to that from the magnetic pickup loops used for the feedback signal.

Chapter 2. Theory

2.1 Magnetohydrodynamic Description of the Plasma-- The Grad-Shafranov Equation

For a static equilibrium, the MHD equations that model the plasma are:

$$2.1 \quad \nabla \cdot \bar{B} = 0$$

$$2.2 \quad \nabla \times \bar{B} = \mu_0 \bar{J}$$

$$2.3 \quad \bar{J} \times \bar{B} = \nabla p$$

B = magnetic field in plasma
J = plasma current
p = plasma pressure

This system of equations in variables \bar{B} , \bar{J} , and p can be reduced to a single variable partial differential equation, the Grad-Shafranov equation. The most direct derivation seems to be that of J. Freidberg [1], and is outlined as follows. (A more complete description is given in Appendix I.) Toroidal geometry is used, with major radius R and toroidal angle ϕ , and with minor radius r and azimuthal angle θ . Appendix I illustrates the coordinate system. ϕ -symmetry is assumed. The stream function ψ is defined, and 2.1 can be expressed in the form (with $\partial/\partial\phi = 0$):

$$2.4 \quad \bar{B} = B_\phi \hat{e}_\phi + \frac{1}{R} \nabla \psi \times \hat{e}_\phi$$

In particular, the poloidal component is given by

$$2.4a \quad B_\theta = \frac{1}{R} \frac{\partial \psi}{\partial r}.$$

With this definition of ψ , the ϕ -component of the vector potential \bar{A} is given by $\psi = RA_\phi$. Further, Equation 2.2 gives

$$2.5 \quad \mu_0 \bar{J} = -\frac{1}{R} \Delta^* \psi \hat{e}_\phi + \frac{1}{R} \nabla(RB_\phi) \times \hat{e}_\phi$$

where the operator Δ^* is defined in Equation 2.8. Equation 2.3 is next broken into three components, in directions parallel to \bar{B} , \bar{J} , and ∇p . $\bar{B} \cdot \nabla p = \bar{B} \cdot (\bar{J} \times \bar{B}) = 0$ results in $p = p(\psi)$, since B is only a function of ψ from Equation 2.4. Similarly, use of Equation 2.5 and $\bar{J} \cdot \nabla p = 0$ results in the formula:

$$\frac{1}{R} \frac{dp}{d\psi} [\nabla(RB_\phi) \times \nabla \psi] \cdot \hat{e}_\phi = 0,$$

$$\text{or } 2.6 \quad RB_\phi = F(\psi).$$

From the above relations, the Grad-Shafranov equation can be derived, and is:

$$2.7 \quad \Delta^* \psi = -\left[\mu_0 R^2 \frac{dp}{d\psi} + F \frac{dF}{d\psi} \right]$$

with:

$$2.8 \quad \Delta^* \psi = \frac{1}{r} \frac{\partial}{\partial r} r \frac{\partial \psi}{\partial r} + \frac{1}{r^2} \frac{\partial^2 \psi}{\partial \theta^2} - \frac{1}{R} \left(\cos \theta \frac{\partial \psi}{\partial r} - \frac{\sin \theta}{r} \frac{\partial \psi}{\partial \theta} \right).$$

2.2 Solutions to the Grad-Shafranov Equation

In the preceding derivation, the pressure p was found to be a function of only the poloidal flux function ψ . Such a quantity is constant on a magnetic flux surface, and is called a surface quantity; another is RB_ϕ . In this work, the high thermal conductivity parallel to the toroidal field has been assumed to imply that flux surfaces are isothermal, and therefore density is a surface quantity as well.

The Grad-Shafranov equation is nonlinear in ψ ; analytic solution requires an expansion in some small parameters. For a typical tokamak, the parameter r/R (= minor radius/major radius) results in an analytically tractable set of equations. In the Alcator Tokamak, this quantity is at most .16/.64. A self-consistent expansion is achieved by taking the toroidal field to be zero order, with the plasma poloidal field $B_{\theta 0} \sim O((\frac{r}{R})^2 B_{\phi 0})$. The diamagnetism $B_{\phi 2}$ is also of this order, as is β , the ratio of plasma energy density $nK(T_e + T_i)$ to magnetic field energy density $B^2/2\mu_0$. Another quantity, $\beta_{pol} = 2\mu_0 nKT / B_\theta^2$, is of order unity.

This equation is solved for a zero-order ψ_0 , which is independent of θ . This is then subtracted from the full Grad-Shafranov equation, and the remaining first order equation is solved iteratively for a small quantity ψ_1 . Since the zero order flux function depends only on the minor radius coordinate r , surfaces of $\psi_0 = \text{constant}$ are circular, as are the zero order terms of all quantities which are solely functions of ψ .

With this expansion, any surface quantity Q can be expressed as $Q = Q_0 + Q_1$, where Q_1 is the first-order correction to Q_0 . It follows that:

$$\begin{aligned} Q(\psi) &= Q_0 + Q_1 \\ 2.9 \quad &= Q(\psi_0) + \psi_1 \frac{\partial Q}{\partial \psi}, \end{aligned}$$

where the second term on the right is defined to be Q_1 . An alternate form, using Equation 2.4a, is

$$\begin{aligned} Q &= Q_0 + \left(R \frac{\partial r}{\partial \psi}\right) \frac{1}{R} \frac{\partial Q}{\partial r_0} \psi_1 \\ 2.10 \quad &= Q_0 + \frac{1}{RB_\theta} \frac{dQ}{dr_0} \psi_1. \end{aligned}$$

Also $RB_\phi = F(\psi)$ results in

$$2.11 \quad B_\phi = \left(\frac{R}{R_0}\right) (B_{\phi 0} + B_{\phi 2}(\psi))$$

as an expression for the toroidal field. $B_{\phi 0}$ is a constant, while $B_{\phi 2}(\psi)$ is introduced to represent the plasma para- or diamagnetism.

2.2.1 One-Dimensional Pressure Balance (Zero-Order)

Neglecting terms of order r/R , the Grad-Shafranov equation is :

$$2.12 \quad \frac{1}{r} \frac{\partial}{\partial r} r \frac{\partial \psi}{\partial r} = -\mu_0 R^2 \left(\frac{\partial p_0}{\partial \psi_0} \right) - \frac{1}{2} \frac{d}{d\psi_0} (R B_\phi)^2$$

By use of Equation 2.4a, this becomes:

$$2.13 \quad \frac{B_\theta^2}{\mu_0 r} + \frac{\partial}{\partial r} \left(\frac{B_\theta^2}{2\mu_0} + p + \left(\frac{R}{R_0} \right)^2 \frac{B_\phi^2}{2\mu_0} \right) = 0$$

which is the one-dimensional pressure balance equation in toroidal geometry. An alternative form, using Equation 2.11, is

$$\frac{B_\theta^2}{\mu_0 r} + \frac{\partial}{\partial r} \left(\frac{B_\theta^2}{2\mu_0} + p + \frac{B_\phi^2 B_\phi^2}{\mu_0} \right) = 0$$

which is readily shown to be equivalent to the pressure balance equation in straight cylindrical geometry.

With this expansion, any surface quantity Q can be expressed as $Q = Q_0 + Q_1$, where Q_1 is the first-order correction to Q_0 . It follows that:

$$Q(\psi) = Q_0 + Q_1$$

$$= Q(\psi_0) + \psi_1 \frac{\partial Q}{\partial \psi}$$

The second term on the right is defined to be Q_1 . Another form, using Equation 2.4a, is

$$Q = Q_0 + \left(R \frac{\partial r}{\partial \psi} \right) \frac{1}{R} \frac{\partial Q}{\partial r} \psi_1$$

$$= Q_0 + \frac{1}{RB_\theta} \frac{dQ}{dr} \psi_1$$

$\rho = F(\psi)$ results in

$$B_\phi = \left(\frac{R}{R_0} \right) (B_{\phi 0} + B_{\phi 2}(\psi))$$

Expression for the toroidal field. $B_{\phi 0}$ is a constant, $B_{\phi 2}(\psi)$ is introduced to represent the plasma parameter perturbation.

-Order)

is

le

-order

$$\theta \frac{dp_0}{d\psi_0}$$

see

ing the

maxima-

ie of

ts

$$B_\theta$$

qua-

Separation of variables can be used to obtain the particular solution $\mathcal{Y}_1 = \psi_1(r) \cos \theta$. (The homogeneous solutions represent non-circularity, see the next section.) This equation can be integrated to obtain an analytic $\psi_1(r)$ [1].

Multiplying through by rB_θ , and making use of the identities

$$\frac{B_\theta}{r} + r \frac{d}{dr} \frac{1}{r} \frac{d}{dr} (rB_\theta) = (rB_\theta)'$$

$$\begin{aligned} \text{and } [rB_\theta^2 \left(\frac{\psi_1}{B_\theta}\right)']' &= [rB_\theta \psi_1' - r \psi_1 B_\theta']' \\ &= B_\theta (r \psi_1')' - \psi_1 (rB_\theta)'. \end{aligned}$$

the differential equation to be solved reduces to:

$$2.17 \quad (rB_\theta^2 \left(\frac{\psi_1}{B_\theta}\right)')' = rB_\theta^2 - 2\mu_0 r^2 \frac{dp_0}{dr},$$

Here $Q' = dQ/dr$. Two integrations give:

$$2.18 \quad \frac{\psi_1}{B_\theta} = \int \left(\frac{1}{2} \frac{\bar{B}_\theta^2}{B_\theta^2} + \frac{\bar{p} - p}{B_\theta^2 / 2\mu_0} \right) r \, dr + \int \frac{C_1}{r B_\theta^2} \, dr + C_2,$$

the equation for ψ_1 . \bar{Q} = the average of a quantity Q , and is defined:

$$2.19 \quad \bar{Q} = \frac{2}{r^2} \int_0^r Q r' \, dr'.$$

The term involving C_1 corresponds to a singularity (i.e., a wire or particle beam) at the plasma center, and in this analysis is set to 0. The boundary condition at the edge of the

plasma is that the radial field = 0, or equivalently $\psi =$ constant ($= \psi_0 + \psi_1 \cos \theta$). Nonzero C_2 is necessary to achieve this, since $\psi_1(r=a) = 0$ is required. Defining the internal inductance and poloidal beta as functions of the minor radius:

$$2.20 \quad l_i = \frac{\overline{B_\theta^2}}{B_\theta^2}$$

$$2.21 \quad \beta_{pol} = \frac{2\mu_0(\bar{p} - p)}{B_\theta^2}$$

results in the final equation for $\psi_1(r, \theta)$:

$$2.22 \quad \psi_1 = B_\theta \left(\frac{l_i}{2} + \beta_{pol} \right) r dr + C_2 B_\theta \cos \theta.$$

This perturbation to ψ_0 can be shown to represent the flux surface shift $\Delta(r)$ derived by Shafranov [4]. By assuming that the equation for a surface on which $\psi =$ constant is given by $r_s = r + \Delta(r) \cos \theta$, then $\psi(r_s) = \psi_0(r_s) + \psi_1(r_s)$ gives (through a Taylor series approximation):

$$2.23 \quad \psi = \psi_0(r) + \frac{d\psi_0}{dr} \Delta \cos \theta + \psi_1(r) \cos \theta.$$

$\Delta(r)$ is the small deviation of the surface from circular. Since the left side is assumed constant, and $\psi_0(r) \neq f(\theta)$,

$$2.24 \quad \psi_1(r) = - \frac{d\psi_0}{dr} \Delta(r).$$

When 2.4a is used to eliminate $\partial\psi_0/\partial r$,

$$2.25 \quad \Delta(r) = - \frac{\psi_1(r)}{R_0 B_\theta} = - \int_0^r \left(\frac{l_i}{2} + \beta_{pol} \right) \frac{r}{R_0} dr,$$

where C_2 has been incorporated into the definite integral.

This is equivalent to the expression for $\Delta(r)$ derived by Shafranov.

$\psi_1(r)$ can be calculated numerically by using zero order density, temperature, and current profiles determined from Alcator plasma discharges. A Gaussian temperature distribution is a good approximation to the temperature as measured by the electron cyclotron emission, as shown in Figure 2.1 [2]. Spitzer resistivity is assumed for the plasma, so the current is proportional to $T^{-3/2}$, with the central current density adjusted to give the correct total current. Semicircular density, or parabolic to a weak power, fits the density profile fairly accurately. As measured from the laser interferometer, this profile is compared with the assumed profile in Figure 2.1[3]. (The density measurement is discussed in Chapter 4.) In summary:

$$\begin{aligned} T_{e,i} &= T_0 \exp(-r^2/a_t^2) \\ J(r) &= J_0 \exp(-3r^2/2a_t^2) \\ n_{e,i} &= n_0 (1 - r^2/a_L^2)^{1/2}, \end{aligned}$$

where a_t and a_d are determined empirically. $B_\theta(r)$ is computed from $J(r)$.

For these profiles, variables $\beta_{pol}(r)$ and $l_i(r)$ are shown in Figure 2.2. These are the quantities which are numerically integrated to obtain $\psi_1(r)$ (or $\Delta(r)$).

Note that the quantity that enters the equation for the shift is the pressure, nKT . Since the temperature has a much sharper, narrower profile than the density, the exact functional dependence of the density on radius is not important.

field = 0, or equivalently $\psi = \text{const}$.
 on zero C_2 is necessary to achieve
 s required. Defining the internal
 eta as functions of the minor radius:

$$\frac{\mu_0 (\bar{p} - p)}{B_\theta^2}$$

tion for $\psi_1(r, \theta)$:

$$+ \beta_{pol} r dr + C_2 B_\theta \cos \theta.$$

ψ_0 can be shown to represent the
 derived by Shafranov [4]. By assum-
 a surface on which $\psi = \text{constant}$ is
 θ , then $\psi(r_s) = \psi_0(r_s) + \psi_1(r_s)$
 series approximation):

$$r) + \frac{d\psi_0}{dr} \Delta \cos \theta + \psi_1(r) \cos \theta.$$

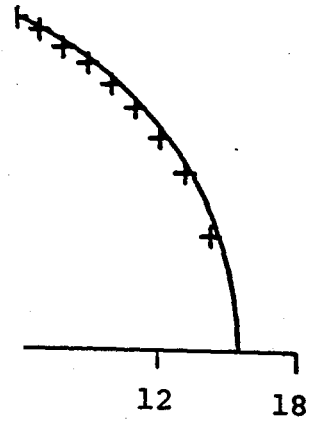
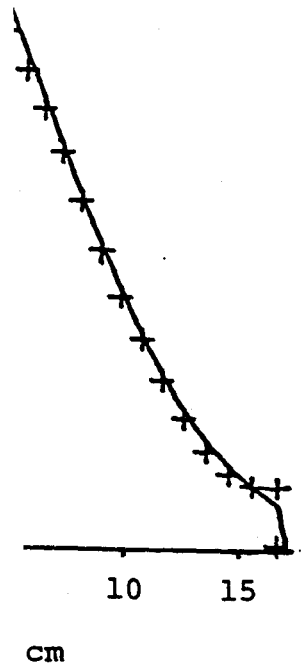
ion of the surface from circular.
 assumed constant, and $\psi_0(r) \neq f(\theta)$,

$$\frac{d\psi_0}{dr} \Delta(r).$$

minate $\partial\psi_0/\partial r$,

$$= - \int_0^r \left(\frac{1}{2} + \beta_{pol} \right) \frac{r}{R_0} dr,$$

porated into the definite integral.



erature and density
 flux surface calcula-
 , while the density is
 gnostics are described

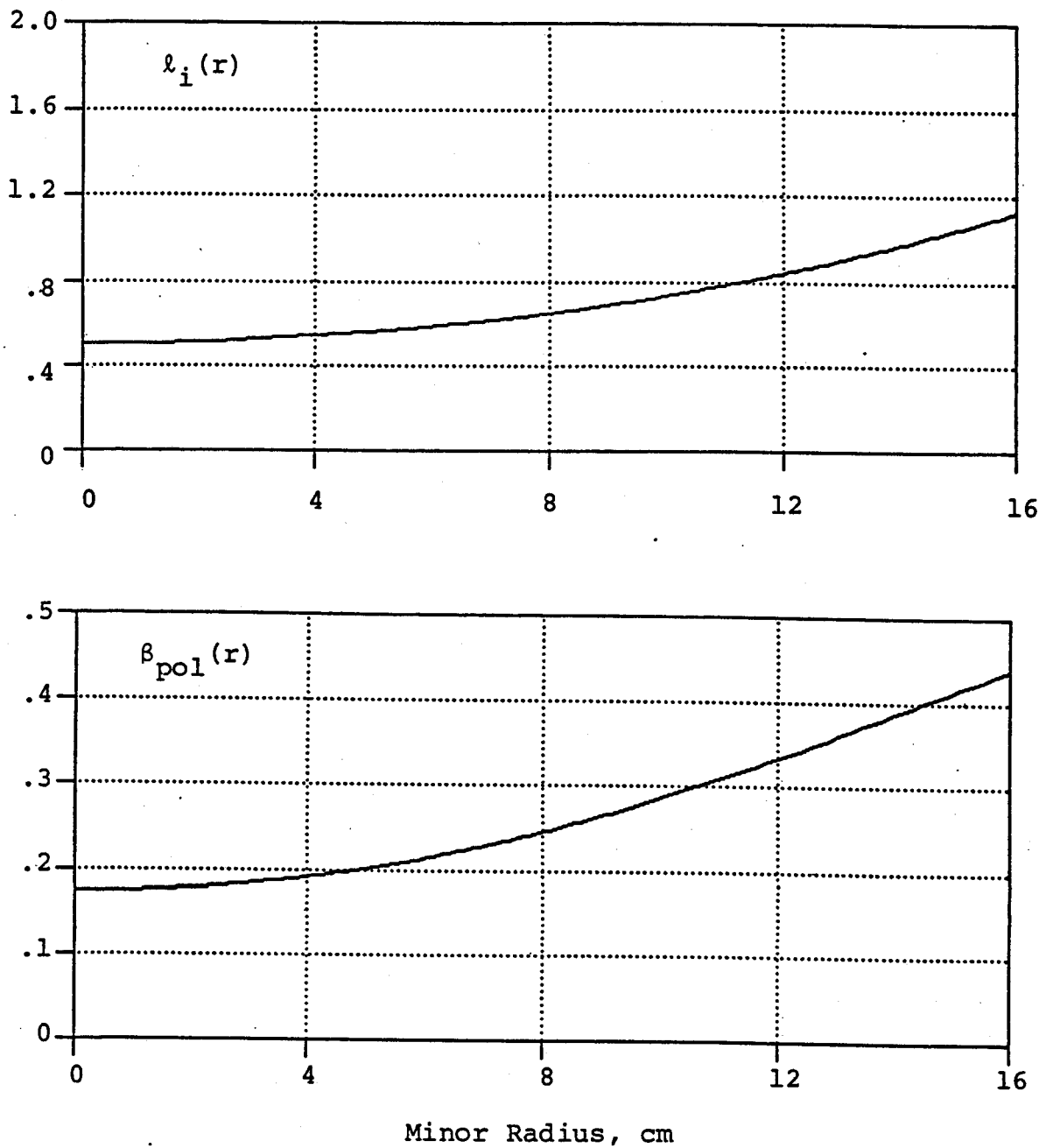


Figure 2.2. The poloidal beta and internal inductance, as functions of radius. These quantities, defined in equations 2.19 and 2.20, are measures of the thermal and magnetic energy internal to the plasma.

For small Δ compared to the minor radius, the equation for flux surfaces represents circles whose centers are offset by the amount $\Delta(r)$. These are plotted in Figure 2.3, with surfaces shown at equi-density intervals. The center of the discharge is shifted outward relative to the outermost flux surface; the predicted displacement is 1.2 to 1.8 cm for typical Alcator C plasmas.

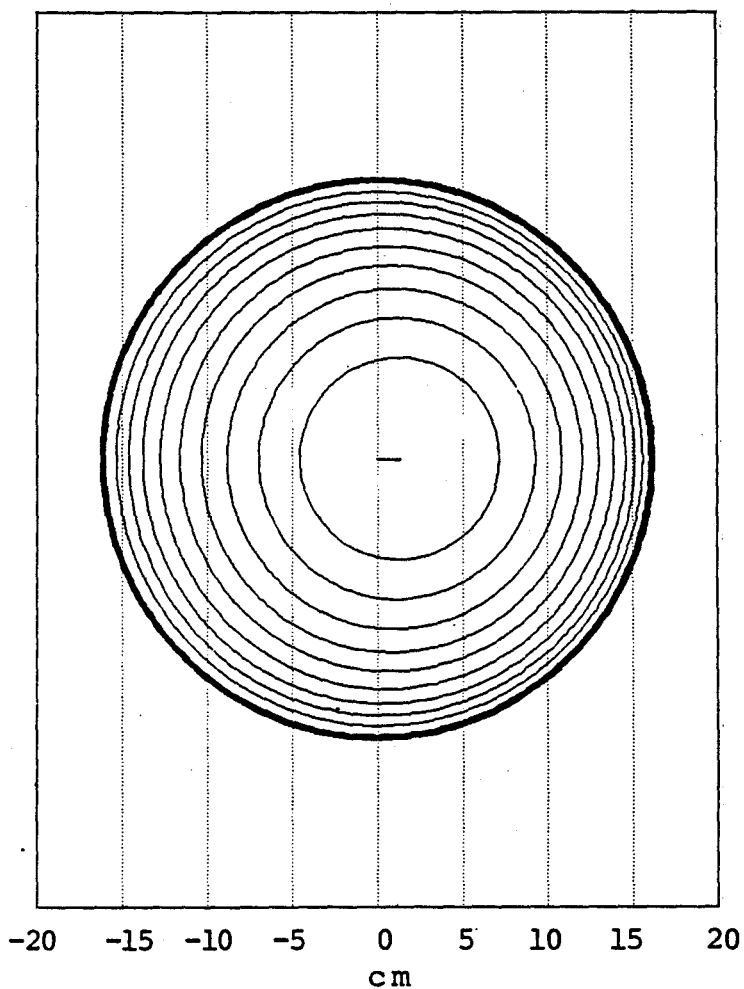


Figure 2.3. The plasma flux surfaces are offset by the amount $\Delta(r)$ with respect to the outermost. This is the "Shafranov shift".

2.2.2.2 Non-Circularity

The vacuum vertical field is not uniformly vertical, but varies across the plasma. Further, there are stray horizontal and vertical fields associated with the main toroidal field; these are cancelled approximately by applied bias fields, but still contain harmonic poloidal field components. With the boundary condition $B_r = 0$ at the plasma edge, these fields result in a first order correction to ψ_0 , in addition to the Shafranov shift. This ψ_{1h} satisfies the homogeneous first-order Grad-Shafranov equation, i.e., solving:

$$2.26 \quad \frac{1}{r} \frac{\partial}{\partial r} \left(r \frac{\partial \psi_1}{\partial r} \right) + \frac{1}{r^2} \frac{\partial^2 \psi_1}{\partial \theta^2} - \frac{1}{B_\theta} \frac{\partial}{\partial r} \left[\frac{1}{r} \frac{\partial}{\partial r} (r B_\theta) \right] = 0.$$

Theta-dependence of the solutions is harmonic, $\psi_{1n}(r, \theta) = \psi_{1n}(r) e^{in\theta}$, but $\psi_{1n}(r)$ must be determined numerically.

Equation 2.26 was solved using backward finite differences. The plots of several solutions are shown in Figure 2.4, with their peak amplitudes normalized to unity (hence the label H_n).

Since the plasma boundary is a constant flux surface, these perturbations to the zero order flux function cause the plasma shape to vary slightly from circular. Mathematically, this is seen by assuming that $r_s = f(r, \theta)$ describes the surface of the plasma, and can be expressed

$$2.27 \quad r_s = a + \sum \delta r_n \cos n\theta.$$

Then, because the surface must be a constant flux surface,

$$\psi = \psi_0(r_s) + \psi_1(r_s) = \text{constant}.$$

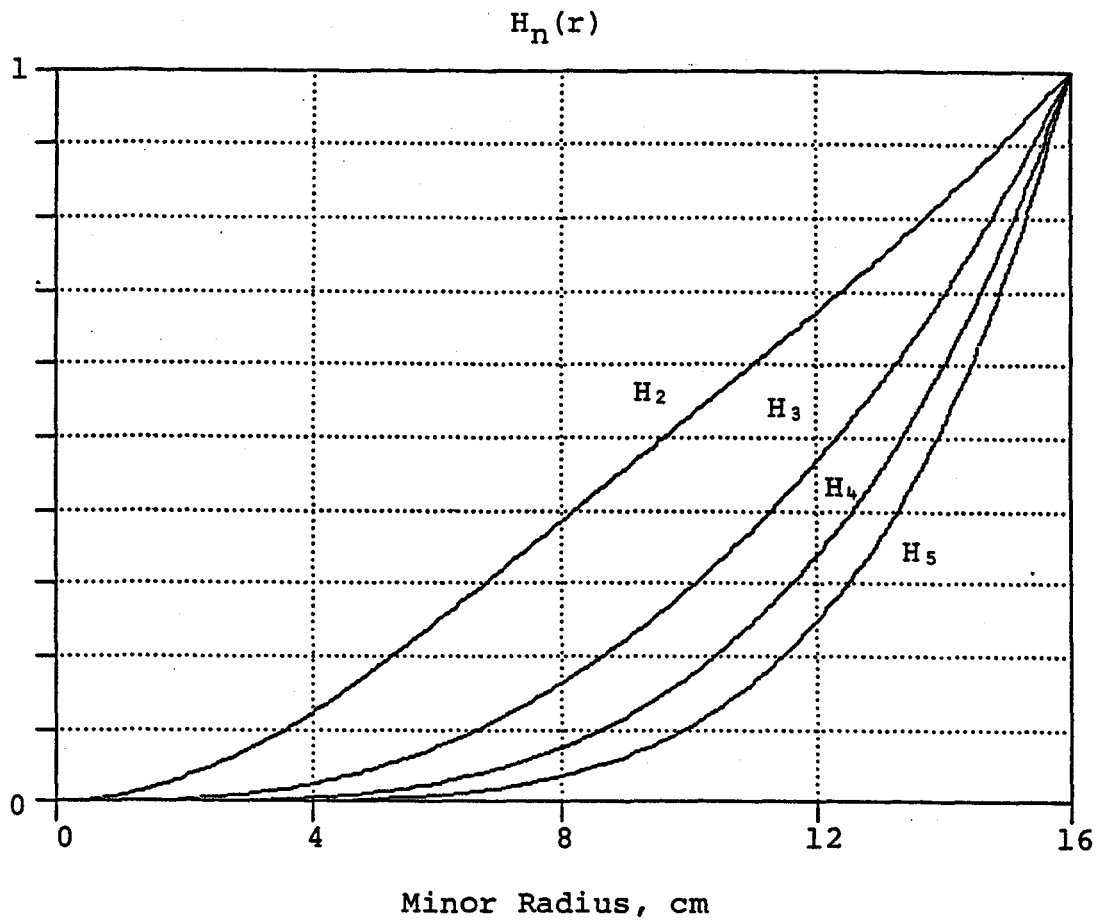


Figure 2.4. Graphs of the first order homogeneous solution of the Grad-Shafranov equation. These are calculated by numerical integration of equation 2.26, and plotted normalized to unity. Boundary conditions at the plasma edge determine the magnitude of each perturbation.

Through a Taylor series expansion, this gives:

$$\psi_{1n}(a) = - \frac{d\psi_0}{dr} \delta r_n \cos n\theta,$$

or 2.28
$$\psi_{1n}(a) = - R_0 B_\theta \delta r_n \cos n\theta.$$

Given the numerical solution of Equation 2.25, described above, values for the δr_n 's may be determined from Equation 2.4a by matching the boundary conditions at the edge of the plasma. The equation for a particular δr_n is:

$$\delta r_n = \frac{B_\theta^{(n)}(a)}{H_1^{(n)}(a)} \cdot \frac{H_1^{(n)}(r)}{B_\theta(r)}.$$

Here $H_1^{(n)}$ represents the calculated flux function perturbations, but with arbitrary normalizations (see Figure 2.4). The magnitudes of these shape perturbations (δr_n 's) are listed in Table 2.1 for several sets of plasma parameters.

When the ψ_{1n} 's are included in the plot of the plasma flux surfaces, deformations are seen to occur at the edge of the plasma, while the center remains virtually circular (Figure 2.5). This is to be expected mathematically, since the perturbation amplitude always increases as a function of radius. Physically, also, it is reasonable that small disturbances in the fields at the edge do not greatly affect the equilibrium in the hotter, higher pressure portion of the discharge. The local ratio of plasma energy to field energy is much greater at the center than at the edge, so small effects in the latter do not propagate inward.

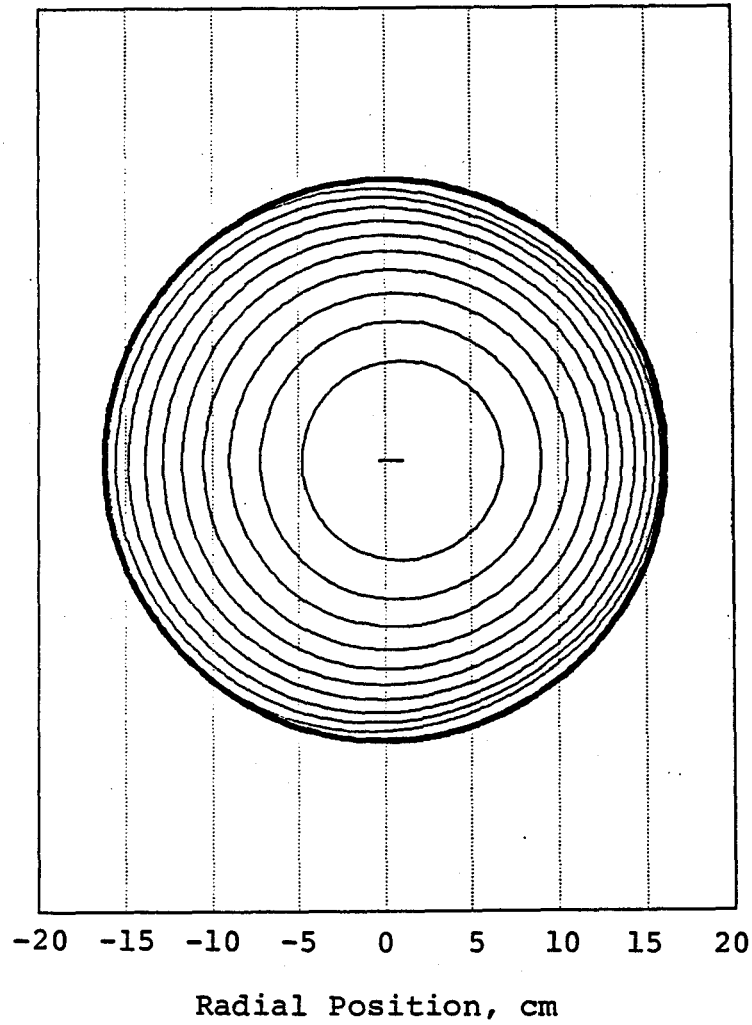


Figure 2.5. Harmonically perturbed flux surfaces. The inhomogeneity of the vacuum vertical field causes perturbations to the shape of the plasma.

The line integral of density through the above-calculated plasma profile is shown in Figure 2.6. The peak is moved slightly outside of center, and the shape made slightly asymmetric. Also shown is the data from a centered Alcator plasma, with an even polynomial function fit to it. In general, the resolution of the density interferometer is probably not great enough to detect the small Shafranov-type perturbations to the density profile. Chapter 4 contains a comparison of the empirical data to results of the calculations performed above.

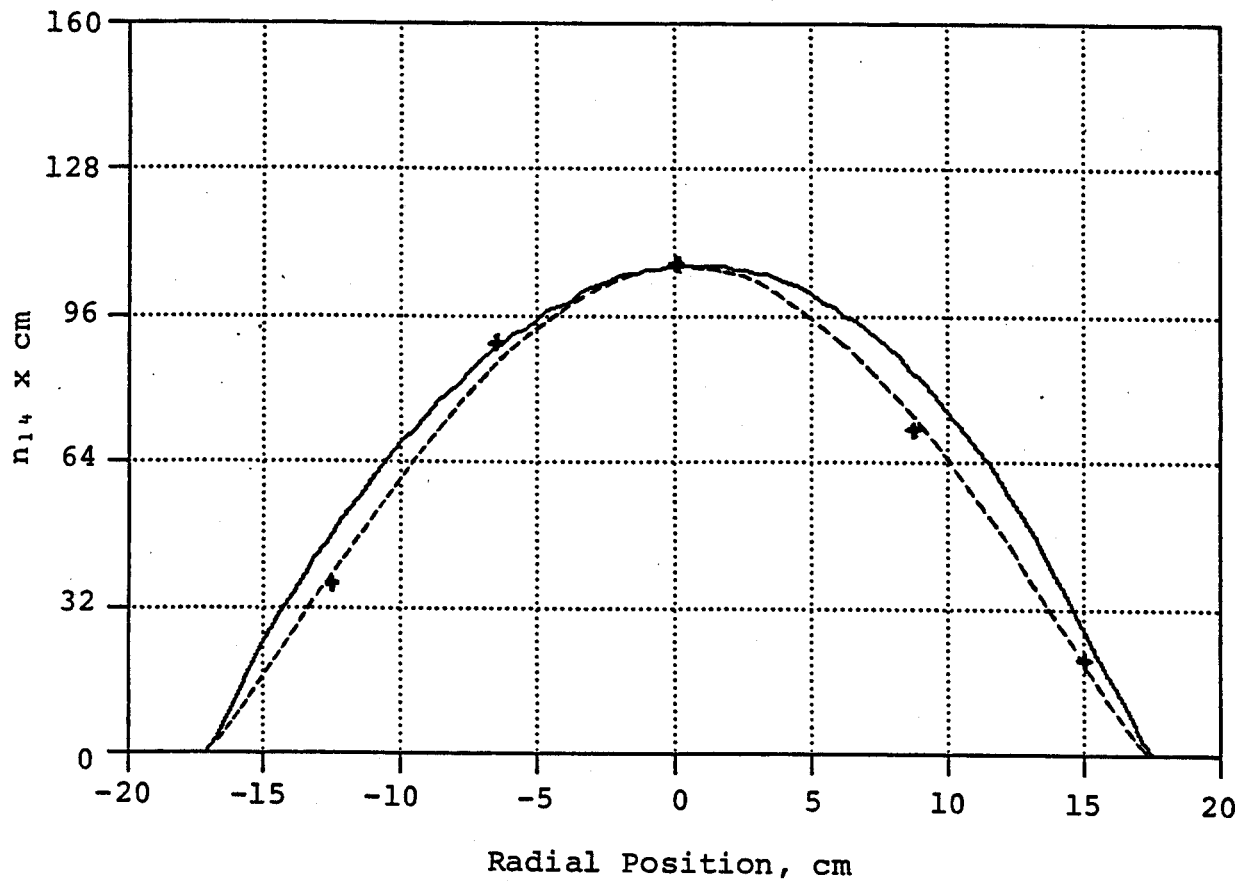


Figure 2.6. Interferometer density data (+'s) compared with the theoretical line integral of the density. The dashed line is an even polynomial that is fit to the data prior to its Abel inversion. To date, the density profile data is consistently symmetric about a midpoint, and the even polynomial fit is well justified. The theoretical profile includes effects from the Shafranov shift and noncircularity, resulting in its asymmetry about the origin.

Table 2.1. Plasma Shape Perturbations from Circular, for Various Plasma Parameters

The following are harmonic radial perturbations of the outer flux surface, with the zero order radius = 16 cm. The surface is given by the equation

$$r_s = 16 \text{ cm} + \sum A_n \cos n\theta + B_n \sin n\theta,$$

with A_n and B_n given in centimeters. The various plasma parameters for each calculated equilibrium are:

I_p = Plasma current, in kA

T_o = peak temperature, in keV, for Gaussian profile

N_o = Peak density, in cm^{-3} , for semicircular density profile of minor radius = 18 cm

B_t = Toroidal field, in Tesla

Shape perturbations are calculated for the toroidal field single turn current both parallel and antiparallel to the plasma current. The single turn is modeled as a Gaussian current distribution of 25 cm width, centered 4 cm above the midplane. Bias fields needed to create a field null in this model are consistent with those actually used to achieve breakdown and plasma centering as of this writing. However, there is evidence that the vertical position of the single turn changes with time.

The only other current used in calculating the field harmonics was that for the vertical field. This was set at a level to give the correct plasma equilibrium.

Table 2.1a The Toroidal Field Single Turn Current is Anti-Parallel to the Plasma Current:

$I_p = 50$	$T_o = .3$	$N_o = 1$	$B_t = 6$		
$n =$	2	3	4	5	6
A_n	-.29	.27	.06	-.03	.01 cm
B_n	.48	-.09	.02	0	0 cm

$I_p = 100$	$T_o = .5$	$N_o = 1.5$	$B_t = 6$		
$n =$	2	3	4	5	6
A_n	.03	.19	.04	-.01	0 cm
B_n	.25	-.04	.01	0	0 cm

$I_p = 200$	$T_o = .75$	$N_o = 3$	$B_t = 6$		
$n =$	2	3	4	5	6
A_n	.22	.15	.03	-.01	0 cm
B_n	.14	-.02	.01	0	0 cm

$I_p = 400$	$T_o = 1$	$N_o = 4$	$B_t = 6$		
$n =$	2	3	4	5	6
A_n	.30	.13	.02	0	0 cm
B_n	.09	-.01	0	0	0 cm

$I_p = 400$	$T_o = 1.2$	$N_o = 5$	$B_t = 9$		
$n =$	2	3	4	5	6
A_n	.24	.14	.03	-.01	0 cm
B_n	.13	-.02	0	0	0 cm

$I_p = 600$	$T_o = 1.2$	$N_o = 5$	$B_t = 9$		
$n =$	2	3	4	5	6
A_n	.27	.12	.02	0	0 cm
B_n	.09	-.01	0	0	0 cm

Table 2.1b The Toroidal Field Single Turn Current is Parallel to the Plasma Current:

$I_p = 50$	$T_o = .3$	$N_o = 1$	$B_t = 6$		

$n =$	2	3	4	5	6
A_n	1.1	-.03	-.01	.03	-.01 cm
B_n	-.5	.09	-.02	0	0 cm

$I_p = 100$	$T_o = .5$	$N_o = 1.5$	$B_t = 6$		

$n =$	2	3	4	5	6
A_n	.72	.04	0	.01	0 cm
B_n	-.26	.04	-.01	0	0 cm

$I_p = 200$	$T_o = .75$	$N_o = 3$	$B_t = 6$		

$n =$	2	3	4	5	6
A_n	.62	.08	.01	.01	0 cm
B_n	-.15	.02	-.01	0	0 cm

$I_p = 400$	$T_o = 1$	$N_o = 4$	$B_t = 6$		

$n =$	2	3	4	5	6
A_n	.54	.08	.01	0	0 cm
B_n	-.09	.01	0	0	0 cm

$I_p = 400$	$T_o = 1.2$	$N_o = 5$	$B_t = 9$		

$n =$	2	3	4	5	6
A_n	.51	.08	.01	0	0 cm
B_n	-.09	.01	0	0	0 cm

$I_p = 600$	$T_o = 1.2$	$N_o = 5$	$B_t = 9$		

$n =$	2	3	4	5	6
A_n	.59	.08	.01	.01	0 cm
B_n	-.12	.02	0	0	0 cm

2.3 The Vertical Field Required for Equilibrium

Due to its toroidal shape, there is a net tendency for the plasma to expand. The magnetic field due to the current ring is greater in the center, so the resultant $\bar{J} \times \bar{B}$ force is outward. Similarly, the distribution of fields inside the current channel itself adds a contribution to the outward force, again since $\bar{J} \times \bar{B}$ is greater on the inside. Third, the internal plasma pressure acts on a greater outward area of the discharge than inward, so isotropic pressure causes a net expansion force. These expansion forces can be counteracted by imposing a vertical field in the vicinity of the plasma; the $\bar{I}_p \times \bar{B}_v$ force can then be adjusted to control the equilibrium position of the plasma.

The fields surrounding a toroidal conductor in the presence of an applied vertical field are given by Mukhovatov [5]

$$2.29 \quad B_{\theta} = \frac{\mu_0 I}{2\pi r} + \left[-\frac{\mu_0 I}{4\pi R} \ln \frac{8R}{r} + \frac{1}{2\pi R} \left(C_2 - \frac{C_1}{r^2} \right) \right] \cos \theta$$

$$2.30 \quad B_r = \left[-\frac{\mu_0 I}{4\pi R} \left(\ln \frac{8R}{r} - 1 \right) + \frac{1}{2\pi R} \left(C_2 + \frac{C_1}{r^2} \right) \right] \sin \theta.$$

The magnitude of the field at infinity is $C_2/(2\pi R)$, representing the applied vertical field. The boundary conditions on B_r and B_{θ} at the plasma edge determine the constants C_1 and C_2 ; $B_r(a) = 0$, while the poloidal field variation $B_{\theta} = B_{\theta}(a)$ is calculated directly from Equation 2.4. Expanding the quantities $\psi = \psi_0 + \psi_1$, $1/R = (1/R_0)(1 - (a/R_0)\cos \theta)$, and $B_{\theta} = B_{\theta 0} + B_{\theta 1}$, and using ψ_1 from the last section, $B_{\theta}(a, \theta)$ can be determined.

Differentiating ψ_1 ,

$$\frac{d\psi_1}{dr} = \left(\frac{l_i}{2} + \beta_{pol} \right) \equiv \Lambda + 1$$

and substituting into Equation 2.4:

$$\begin{aligned} 2.31 \quad B_\theta(a, \theta) &= \frac{1}{R} \frac{d\psi}{dr} = B_{\theta 0} \left(1 - \frac{a}{R} \cos \theta \right) + B_{\theta 1} \\ &= \frac{\mu_0 I}{2\pi a} \left(1 + \frac{a}{R} \Lambda \cos \theta \right). \end{aligned}$$

The fields surrounding the plasma are then (assuming no surface currents at the edge of the plasma):

$$2.32 \quad B_\theta = \frac{\mu_0 I}{2\pi R} + \frac{\mu_0 I}{4\pi R} \left[\ln \frac{r}{a} - 1 + \left(\Lambda + \frac{1}{2} \right) \left(1 + \frac{a^2}{r^2} \right) \right] \cos \theta.$$

$$2.33 \quad B_r = \frac{\mu_0 I}{2\pi r} \left[\ln \frac{r}{a} + \left(\Lambda + \frac{1}{2} \right) \left(1 - \frac{a^2}{r^2} \right) \right] \sin \theta.$$

The vertical field that satisfies the above boundary conditions is

$$2.34 \quad B_v = \frac{C_2}{2\pi R} = \frac{\mu_0 I}{4\pi R} \left(\ln \frac{8R}{a} + \Lambda - \frac{1}{2} \right),$$

and this is the well known expression for the vertical field required by the plasma at equilibrium [1],[4],[5].

The vertical field actually used to center the plasma agrees to experimental error ($\sim 5\%$) with that predicted above.

Chapter 3. The Feedback System

A block diagram of the feedback system is shown in Figure 3.1. An SCR power supply drives a set of four coils, which generate a vertical magnetic field. The $\vec{J} \times \vec{B}$ force of this field on the plasma current acts to position the plasma.

As derived in Chapter 2, the vertical field required for equilibrium radius R is given by

$$2.34 \quad B_v = \frac{\mu_o I_p}{4\pi R} \left(\ln \frac{8R}{a} + \beta_{pol} + \frac{l_i}{2} - 1.5 \right).$$

To a first approximation, the field should be directly proportional to the plasma current; variations in plasma radius a , pressure term β_{pol} , or profile term $l_i/2$ represent disturbances that must be corrected for. In the feedback system, Figure 3.1, the major portion of the programming is a constant times the plasma current, in accordance with the above equation (since $\ln 8R/a$ is 5-10 times β_{pol} or $l_i/2$). The loop error signal is proportional to the deviation of position from the vacuum vessel center, $R = .64$ m, and this is summed with the αI_p contribution to generate the proper field programming signal. Some phase lead is added to increase stability and to improve response of the system to rapid plasma variations; this becomes the input to the SCR power supply. Optional programming of the plasma position is also provided for at the input of the supply, as shown.

Note that for a given change in position, the programming change should be proportional to the plasma current. For

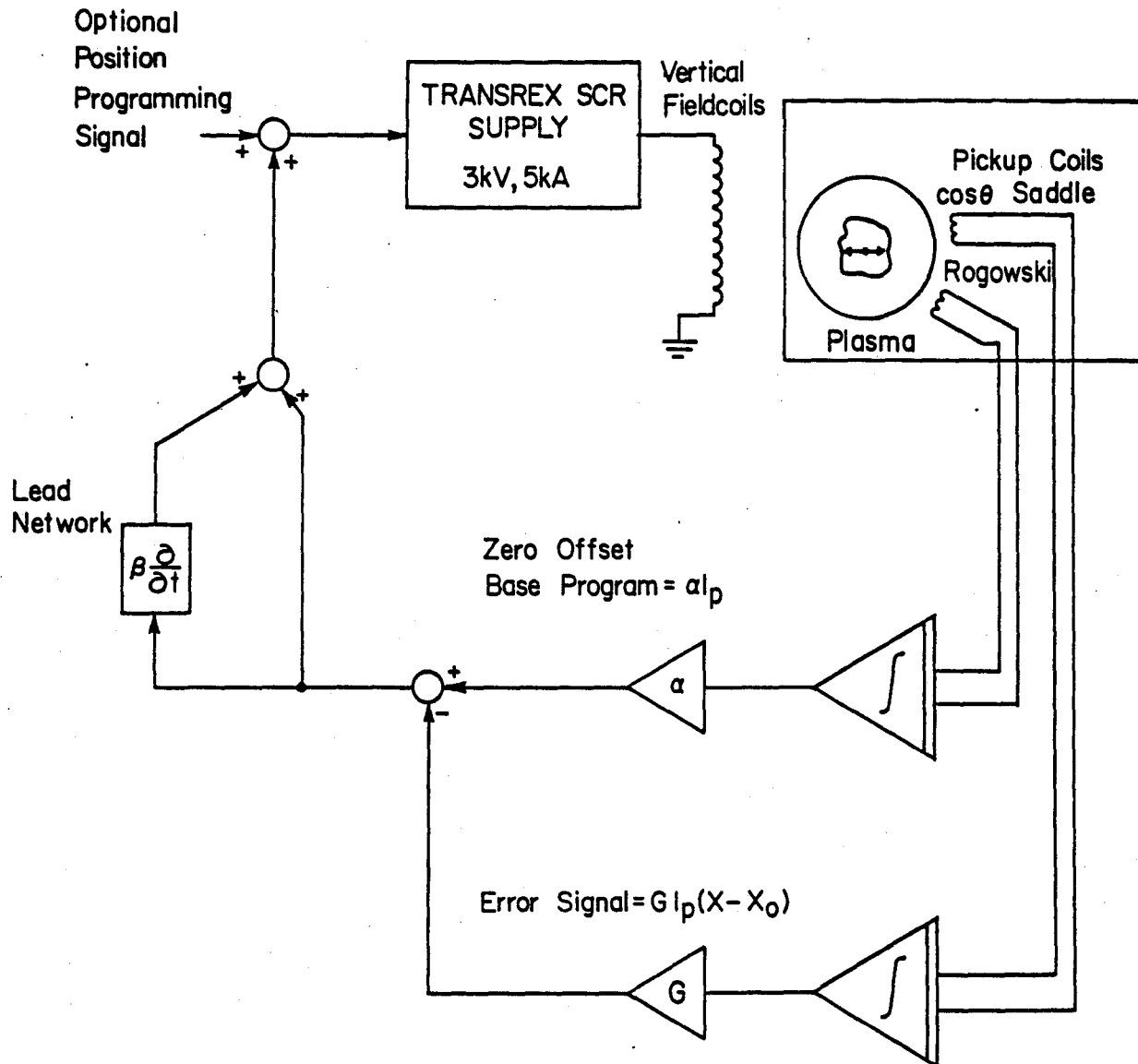


Figure 3.1. The Feedback System. The SCR supply drives the vertical field coils to position the plasma. The plasma current forms the base program for the supply, with the position error signal added as a correction. Optional position programming is allowed, as well.

constant loop gain, the error signal should be the product of position displacement and plasma current, and this is the signal obtained from the pickup loops. Further, a constant offset can be achieved using a signal proportional to the plasma current as the programming signal. In practice, this is done by varying the contribution of the zero order programming, $\propto I_p$.

3.1 A Model of the Feedback Loop

A model of the feedback system is presented for linear analysis in this section. The model is shown in Figure 3.2 (see Figure 3.1 for the actual feedback system). The main components and interactions that are considered are: a) The SCR power supply generates a current in the vertical field coils, which acts to position the plasma; b) variations in plasma parameters such as current, temperature, or profile represent disturbances which must be corrected for; and c) the product of position and current is measured, and forms the error signal in the feedback loop. With an apparent frequency dependence of plasma response to the applied field, the plasma transfer function is proportional to $I_v / (1 + s\tau_p)$. This signal is the input to the feedback electronics, which then drives the SCR supply. An optional position programming signal can also be added to the feedback error signal, as illustrated in Figure 3.2 at V_{prog} .

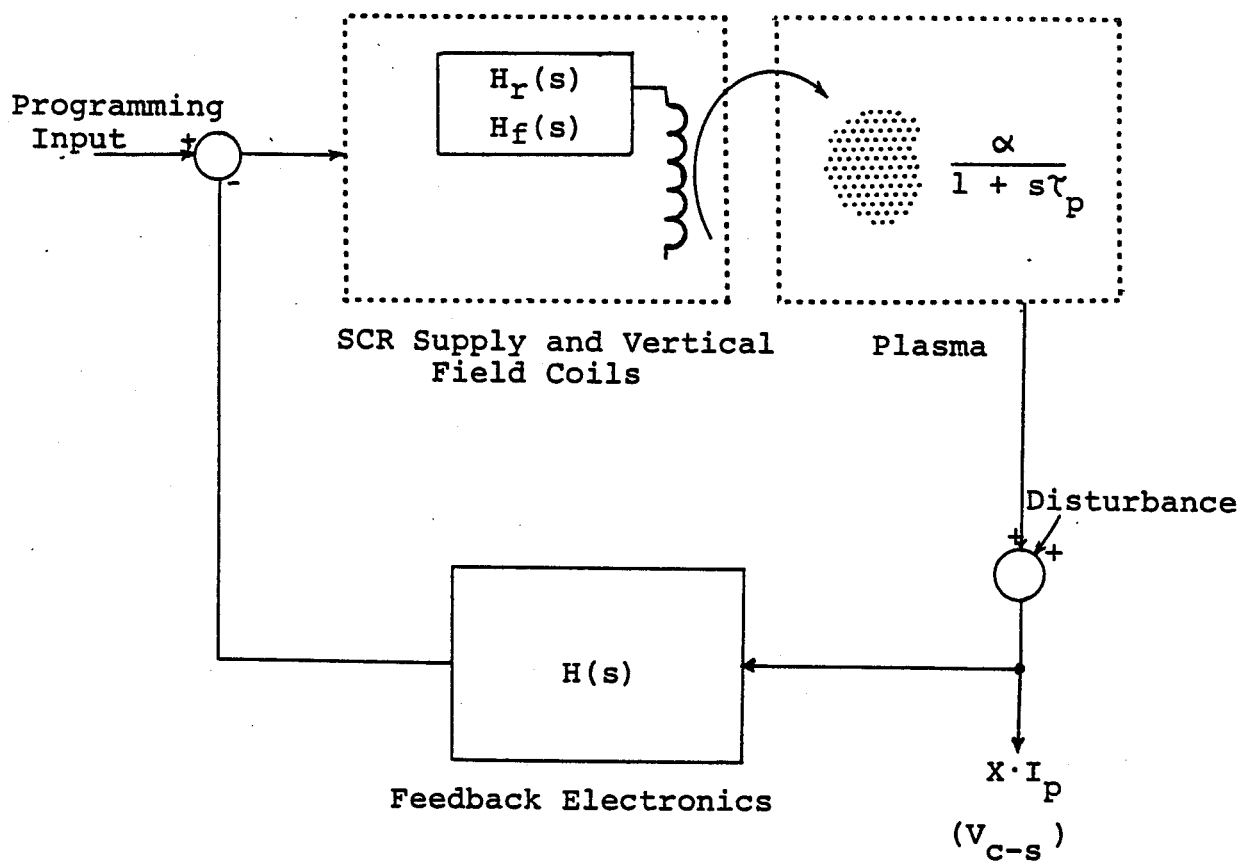
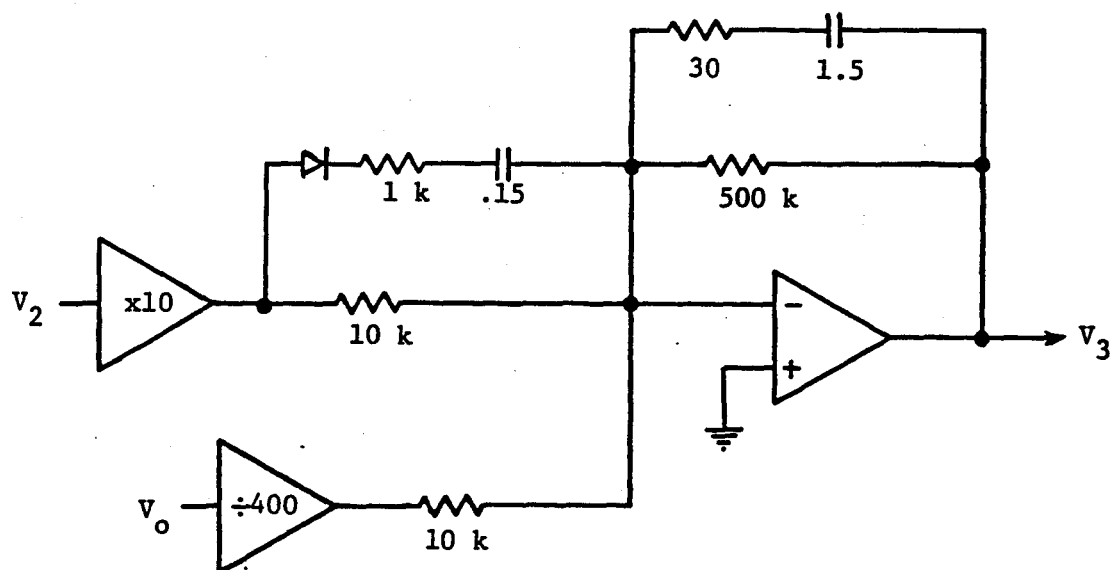


Figure 3.2. A linear model of the feedback loop.

3.1.1 The Vertical Field Power Supply

The vertical field power supply is a three kilovolt, five kiloamp SCR supply used in programmed current mode. A linear model for analyzing the power supply response will be presented in this section, and is shown in Figure 3.3; the supply contains a general division between the internal control electronics and the power output stage, as is indicated in the figure. The control electronics includes a large amount of safety and fault detection circuitry, but the dynamic response is normally independent of these. During linear operation, the internal electronics is essentially represented by the following:



where V_0 , V_2 and V_3 are the same as in Figure 3.3. The output of this stage, V_3 , directly controls the firing times of the SCR gate pulses. The DC gain is 500, with different AC gains for rising and falling input voltage. V_0 is the supply output voltage, and this signal path forms an internal feedback

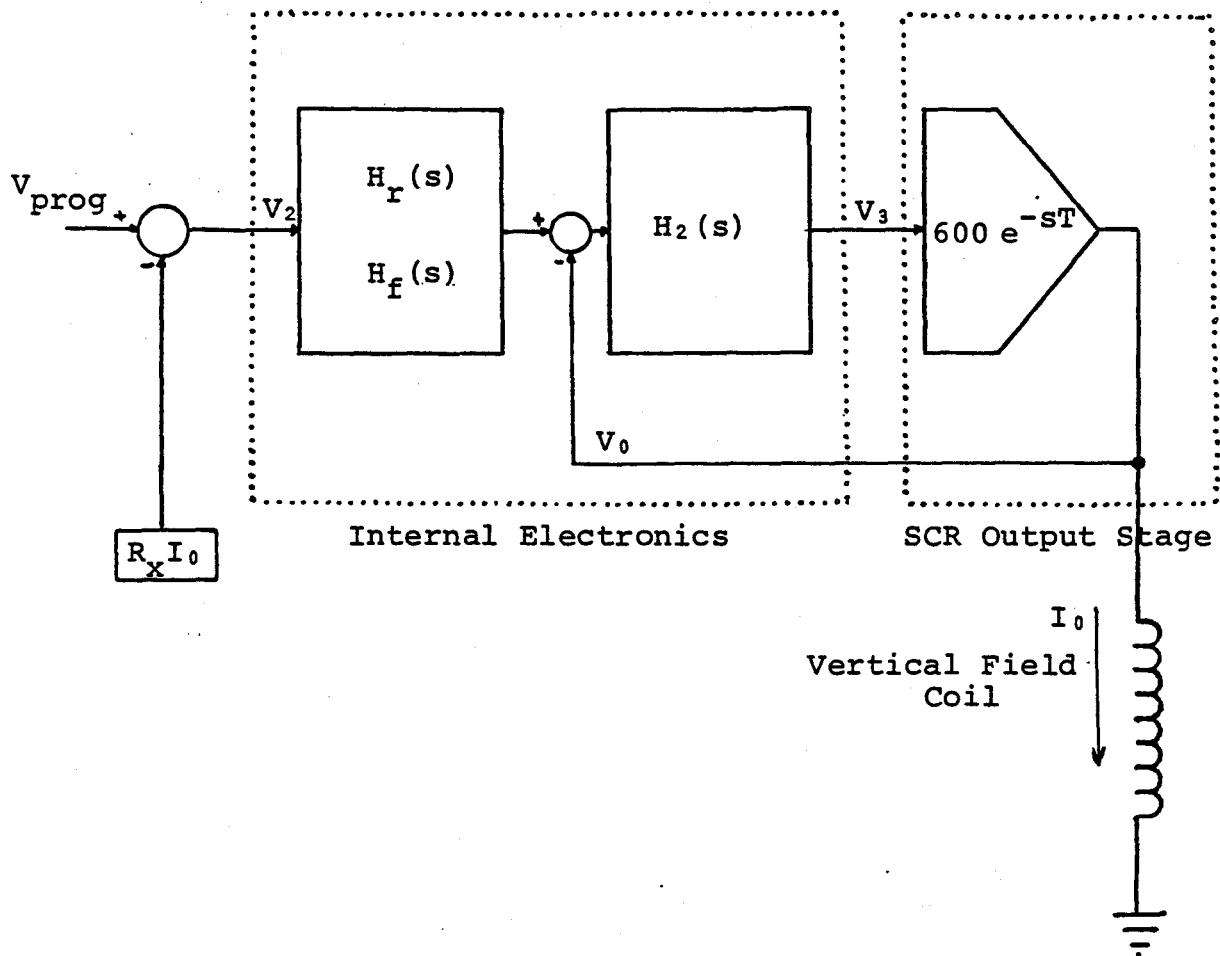


Figure 3.3. A linear model of the vertical field SCR supply. The internal electronics contains a diode in the forward signal path, resulting in separate transfer functions for the cases of rising or falling V_2 . These are denoted by $H_r(s)$ and $H_f(s)$; $H_2(s)$ is $50/(1 + s \times .7 \text{ sec})$. The supply is operated with output current feedback.

loop for voltage control. V_2 is the input programming signal minus the feedback signal (= output current times $.00226\Omega$). There are two forward transfer functions for the above circuit; in the case where the input signal is positive and the diode is biased on, the transfer function includes a lead network:

$$H_r(S) = \frac{1 + .00165 S}{1 + .00015 S}.$$

In the falling input case, or steady state, the transfer function $H_f(s)$ is unity. The next op-amp stage has as its transfer function

$$H(s) = 50 \frac{1 + .000045 s}{.75 s}.$$

The power output stage follows, consisting of a three-phase SCR bridge driven from a 3000 V transformer. There is a delay due to the three-phase line being switched, which can be as great as 2.7 ms. This stage is represented in the model as having a voltage gain of 600, though the actual output is a nonlinear function of the input. The supply output drives the vertical field coils, an inductance of .14 Henry.

The supply is operated in a closed loop configuration, with internal feedback on the output current and voltage. For the model of the supply shown in Figure 3.3 and considered above, the closed loop transfer function is:

$$3.1 \quad H_{\text{Supp}}(s) = \frac{1}{2.26} \frac{H_{\text{rf}}}{2 \times 10^{-4} (1 + .75s)s e^{sT} + .015s + H_{\text{rf}}},$$

where $H_r(s)$ and $H_f(s)$ are the rising- and falling-input transfer functions, and the delay due to the AC line being switched is represented by e^{-sT} . Bode plots of the closed loop response of the supply model are shown in Figure 3.4; plots are given for operation involving both H_r and H_f . The SCR delay is approximated as being 1.4 ms, its average value. (In the supply, there are lowpass filters on the signals V_o and V_2 ; with time constants of .5 ms, these were included for the Bode plot calculations.)

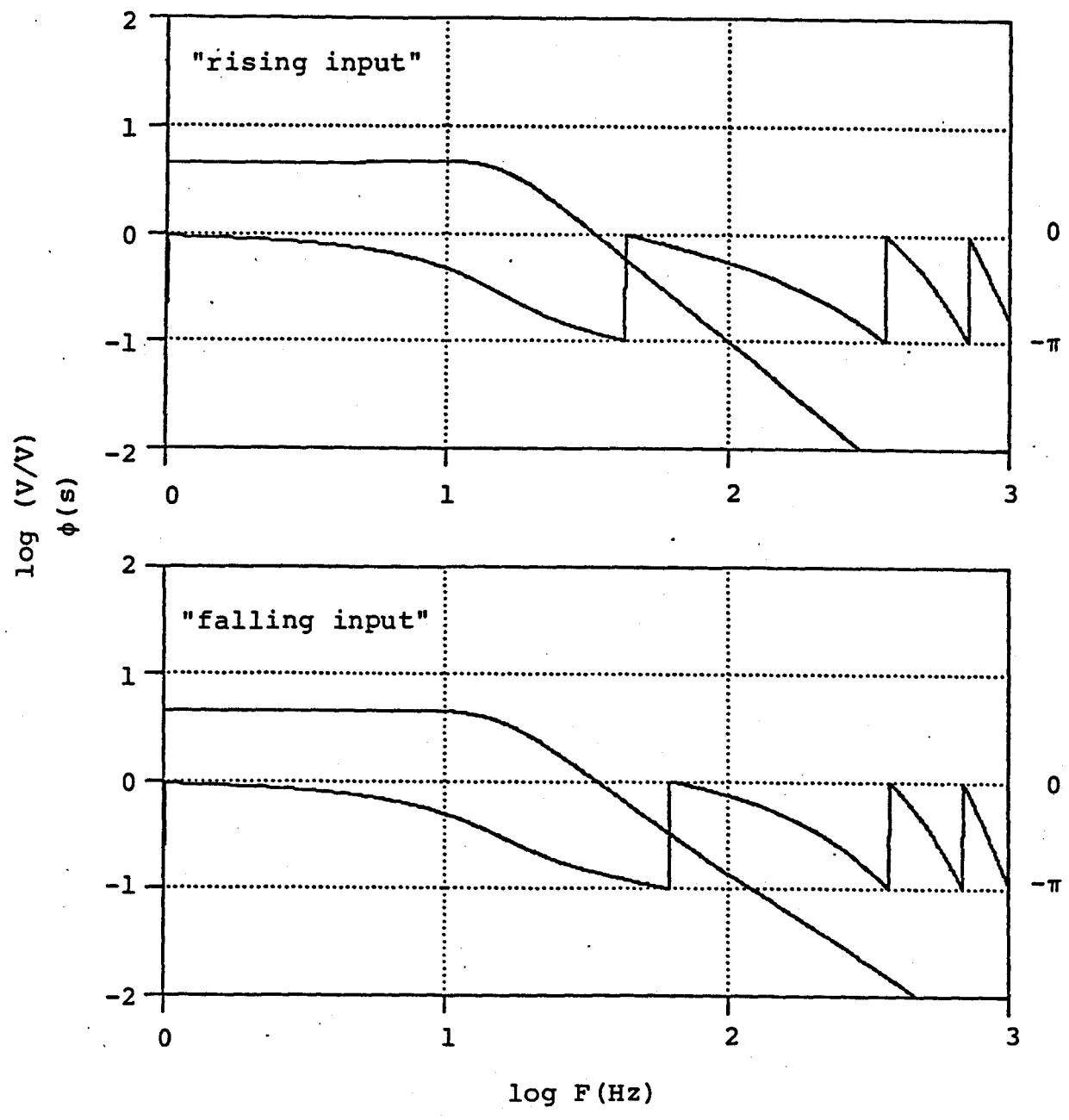


Figure 3.4. Bode plots of the closed loop response of the vertical field power supply (as modeled). The supply has different transfer functions for the cases of a) rising and b) falling inputs to the supply.

3.1.2 The Plasma and Position Sensing Response

The plasma response, as measured by the position-sensitive coils, is:

$$3.2 \quad P(s) = \frac{\alpha}{1 + s\tau_p}$$

$$\text{where } \alpha = \alpha_1 \alpha_2 = 3 \text{ V/kA (vert. field)}$$

$$\alpha_1 = 13 \frac{\text{cm}}{\text{kA}} \frac{100 \text{ kA}}{I_p}, \text{ the plasma response}$$

$$\alpha_2 = .23 \frac{\text{V}}{\text{cm}} \frac{I_p}{100 \text{ kA}}, \text{ the instrumentation response}$$

$$\tau_p = 1.6 \text{ ms.}$$

The time constant τ_p is measured, and is not well understood physically. The observed delay might be a penetration effect of the vertical field through the edge plasma, where the temperature, and therefore the plasma conductivity, is low. The edge plasma is believed to have a temperature of approximately 50 eV, with a density of $5 \text{ to } 10 \times 10^{13} \text{ cm}^{-3}$. This results in the conductivity, $\sigma \approx 2 \times 10^5 (\Omega \cdot \text{m})^{-1}$ [7], and the skin penetration time through 6 cm is about 1 ms. For this reason, the ideal MHD equations used above are of questionable validity in that region of the plasma. Further, in order to neglect viscosity in the MHD description of the plasma, the temperature and density must satisfy the condition [1]:

$$1.6 \times 10^{-4} \frac{T^2(\text{eV})}{n_{14}} \gg 1$$

where T = temperature in electron volts

n_{14} = density / (10^{14} cm^{-3}).

For the low edge temperatures present, this inequality is not

met, and this would add another term to the MHD equations.

In summary, the observed delay is likely to be due to a current redistribution effect in the edge of the plasma, taking place in the region for which the ideal MHD description of the plasma breaks down.

3.1.3 The Feedback Circuit

Without frequency compensation, the closed loop system is unstable when the DC gain is high enough for accurate position control. (The system goes into a limit-cycle oscillation in which the slew rate of the vertical field current, and thus position, is limited by the output voltage of the SCR supply.) Consequently, a lead network is included in the feedback loop. Lead compensation was chosen in order to achieve the fastest closed loop response to a plasma disturbance.

The feedback circuit has a single pole-zero pair transfer function. With adjustable gain and lead, this transfer function is:

$$3.3 \quad H(s) = H_0 \frac{1 + s\tau_1}{1 + s\tau_2}$$

$$\begin{aligned} \text{where:} \quad \tau_1 &= 5.2 \text{ ms (variable)} \\ \tau_2 &= 1 \text{ ms} \\ H_0 &= 2.5 \text{ (variable)}. \end{aligned}$$

τ_1 is the lead parameter, while H_0 represents the DC gain of the circuit. For the actual circuit diagram, see Appendix III.

3.1.4 Stability and Response of the Feedback System

Bode plots of the open loop transmission of the system discussed above are shown in Figure 3.5. The SCR switching of the three-phase line must be taken into account for the stability analysis. Since a disturbance may occur at any time with respect to the line period, this delay is of random length, from 0 to 2.7 ms. The feedback system must be stable in the worst case, i.e., for the longest delay. However, once this is achieved, the system response is best approximated by use of the 1.4 ms average delay. In Figure 3.5a, the loop transmission is plotted for the case of no frequency compensation and with the 2.7 ms delay. This is seen to be unstable for feedback operation, as the gain is greater than unity for a phase of π radians. This instability is observed experimentally; the system goes into the limit cycle oscillation described previously. Figure 4.4 illustrates a plasma shot under these conditions. The normal operating setting of the lead network stabilizes the transfer function, and the Bode plots of Figure 3.5b illustrate this case. For these plots, the delay is set to its average value of 1.4 ms. All Bode plots illustrate both rising and falling inputs to the SCR supply, since the loop transmissions are different for each.

In general, the rising and falling transfer functions may be separated. The dominant input to the SCR supply is proportional to the plasma current, and consists of ramps that are large compared to the position error signal. Operation of the feedback system is described in Chapter 4; for the period

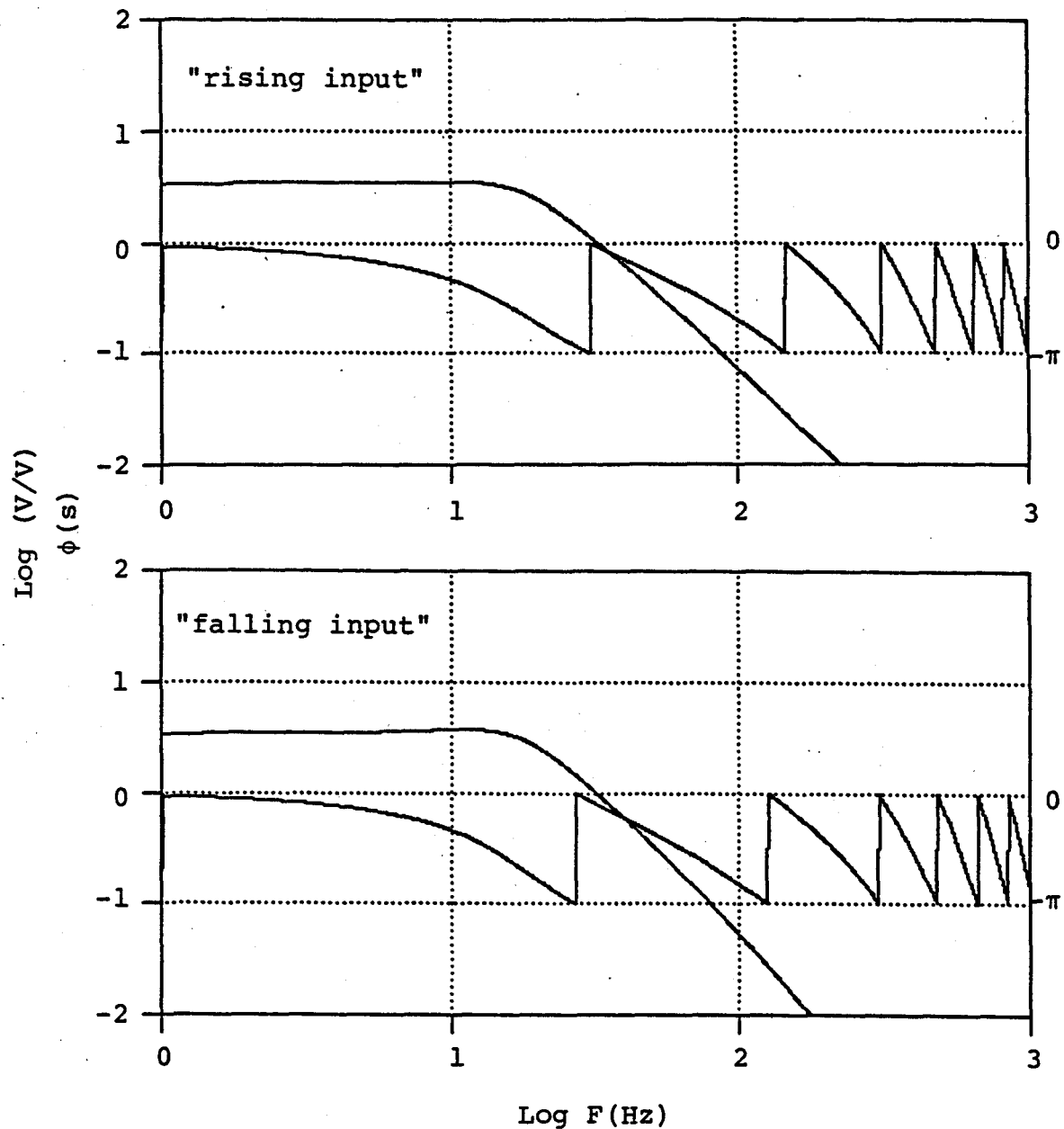


Figure 3.5a. Bode plots of the feedback system open loop transmission (as modeled). The case of no frequency compensation from the feedback circuit results in an unstable closed loop response. Both cases of SCR supply operation are shown (rising and falling inputs as described previously).

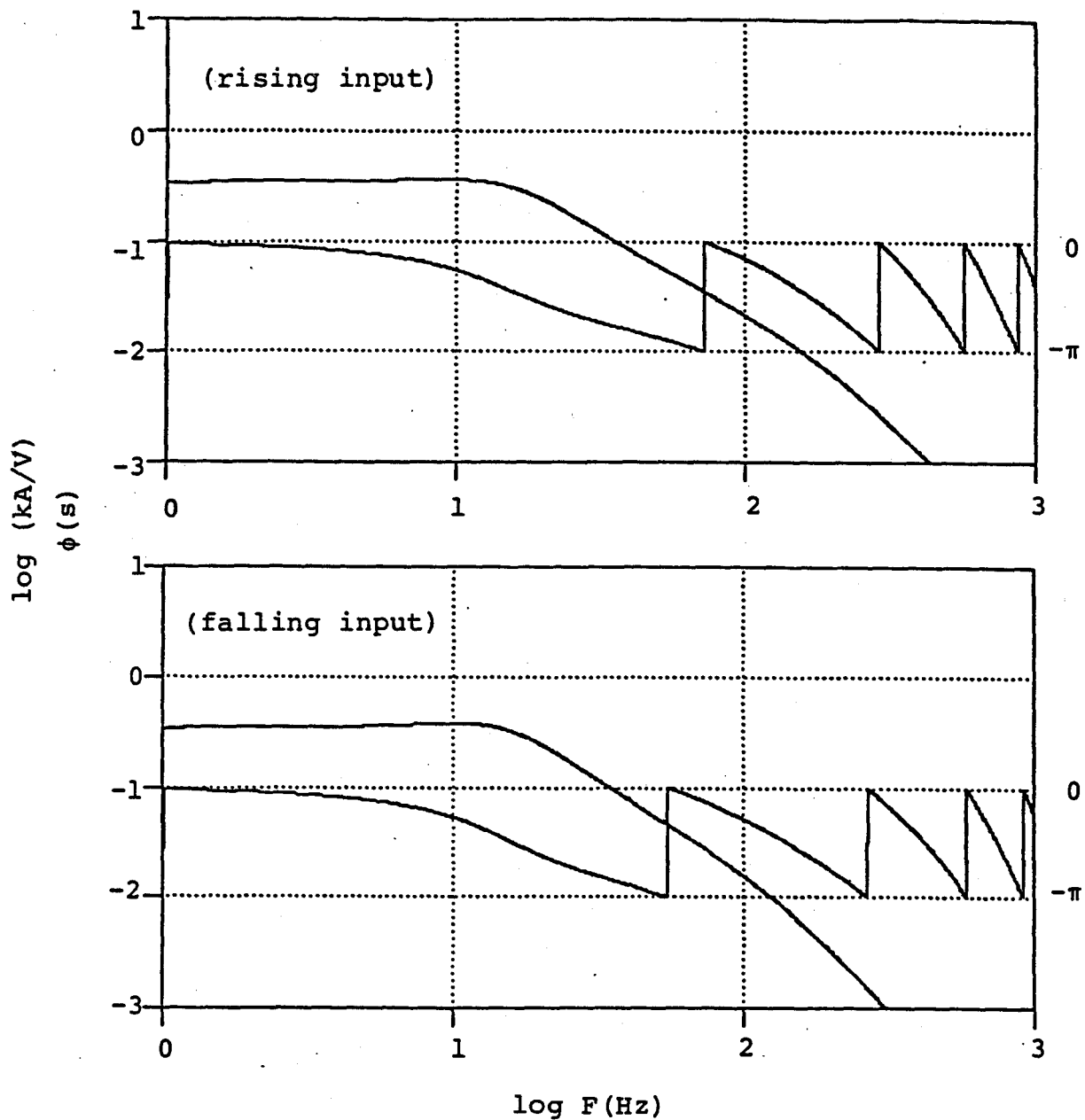


Figure 3.5b. Bode plots of the feedback system open loop transmission (continued). The normal operating settings were used to generate the response plot. Both cases of SCR supply operation are shown.

of the current rise, the "rising input" transfer function is in effect. For current flat-top and fall, the "falling input" case must be used.

The closed loop frequency response calculated for this model is shown in Figure 3.6a. The excitation is a signal at the programming input, and the response is the resulting plasma displacement. Figure 3.6b is a Bode plot of closed loop response to a disturbance in the plasma, as measured by the position-sensing coils. The resonance occurs at about 40 Hz, and this is in reasonable agreement with the measured dynamic response of the feedback system. Feedback system operation is described in Chapter 4.

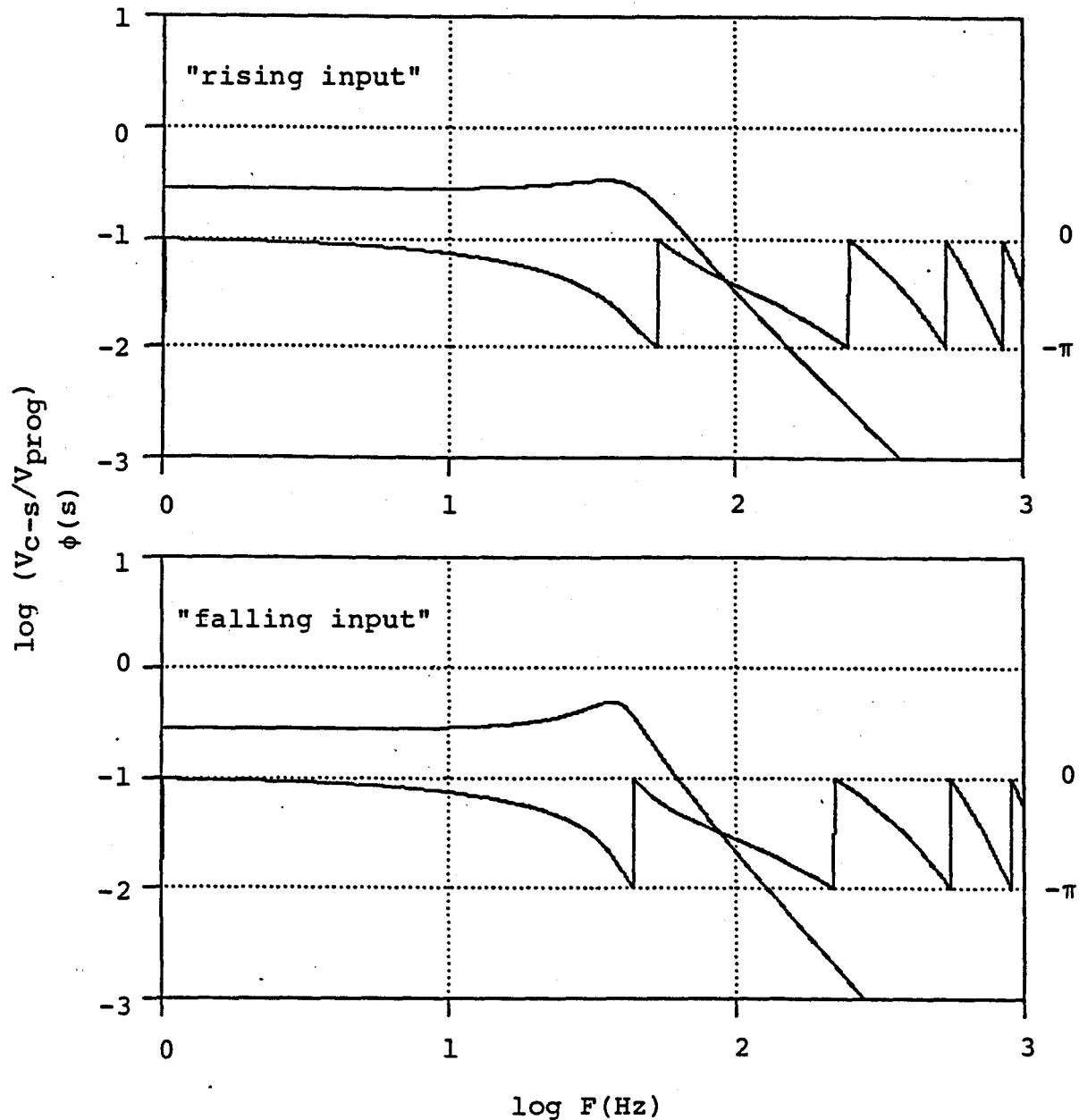


Figure 3.6a. Bode plots of the closed loop frequency response of the feedback system. The excitation is a programming signal, while the response is the measured position signal V_{C-s} . Again, both cases of SCR supply operation are shown.

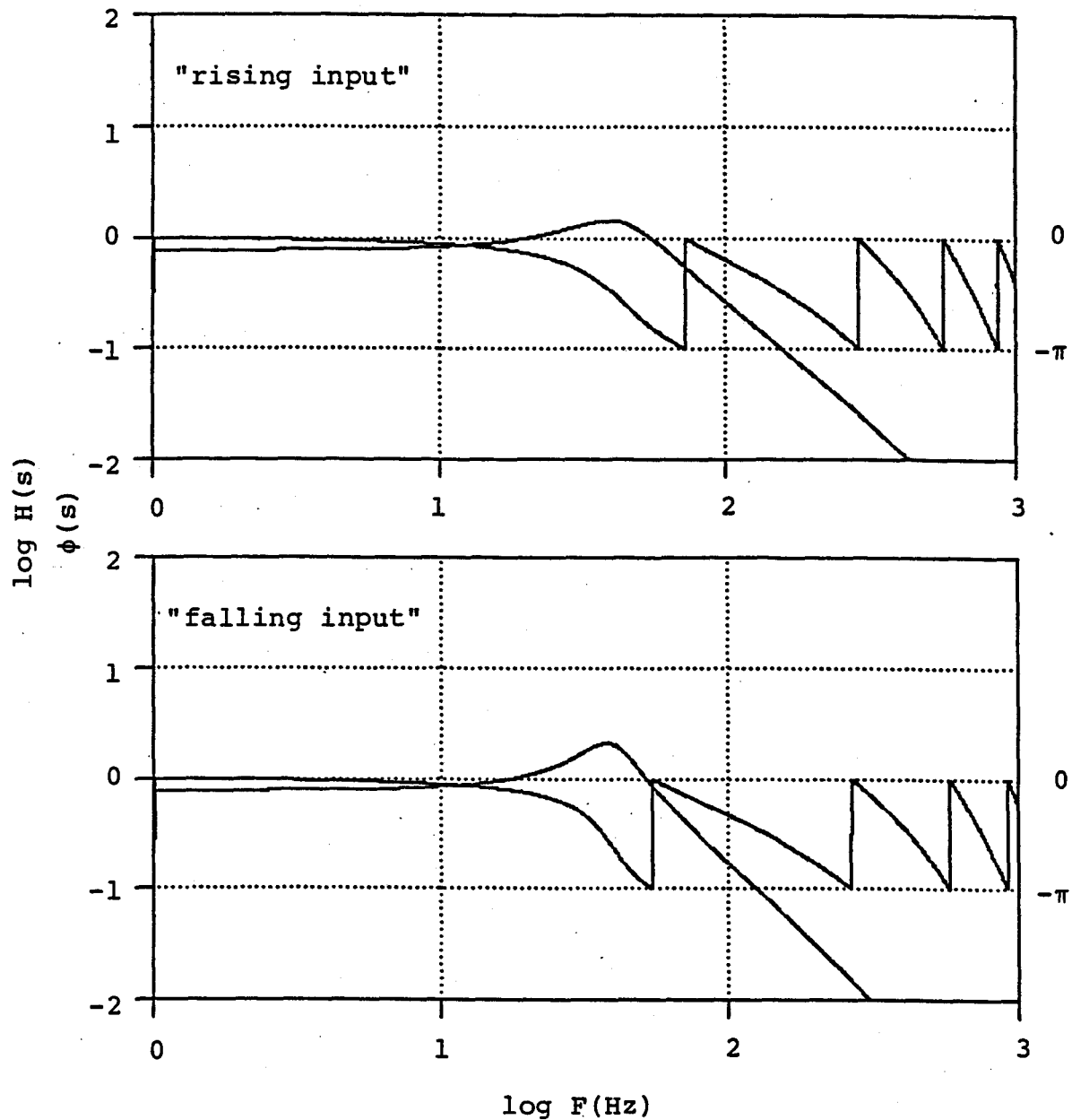


Figure 3.6b. Bode plots of the closed loop frequency response of the feedback system. The excitation is an equivalent plasma disturbance, while the response is the position signal. Both cases of SCR supply operation are shown.

3.2 The Position-Sensing Pickup Coils

These coils are situated just outside the vacuum vessel wall. Both coils produce voltages

$$3.4 \quad V = C_{c,s} \frac{d}{dt} (I_p (X - X_o))$$

where X = plasma position with respect
to the vacuum chamber center
 X_o = offset due to toroidal geometry
 I_p = plasma current
 $C_{c,s}$ = scale factor for either $\cos \theta$
or saddle coil.

These signals are time-integrated to provide position information.

The coils are wound on a flat strip, which is then wrapped around a minor circumference of the torus (see Figure 3.7). The $\cos \theta$ coil is wound to approximate a turns density of $n_o \cos \theta$, and is thus sensitive to poloidal fields with $\cos \theta$ functional dependence. The saddle coil is wound lengthwise on the edges of the strip, crossing over at the center, and its sensitivity is to radial fields B_r at the vacuum chamber surface. Note that since a vertical field in cylindrical coordinates is

$$B_v = B_{v0} (\hat{r} \cos \theta + \hat{\theta} \sin \theta),$$

the $\cos \theta$ and saddle coils detect the net vertical field intersecting the vacuum vessel. To a first approximation, the object of the applied vertical field can be viewed as being

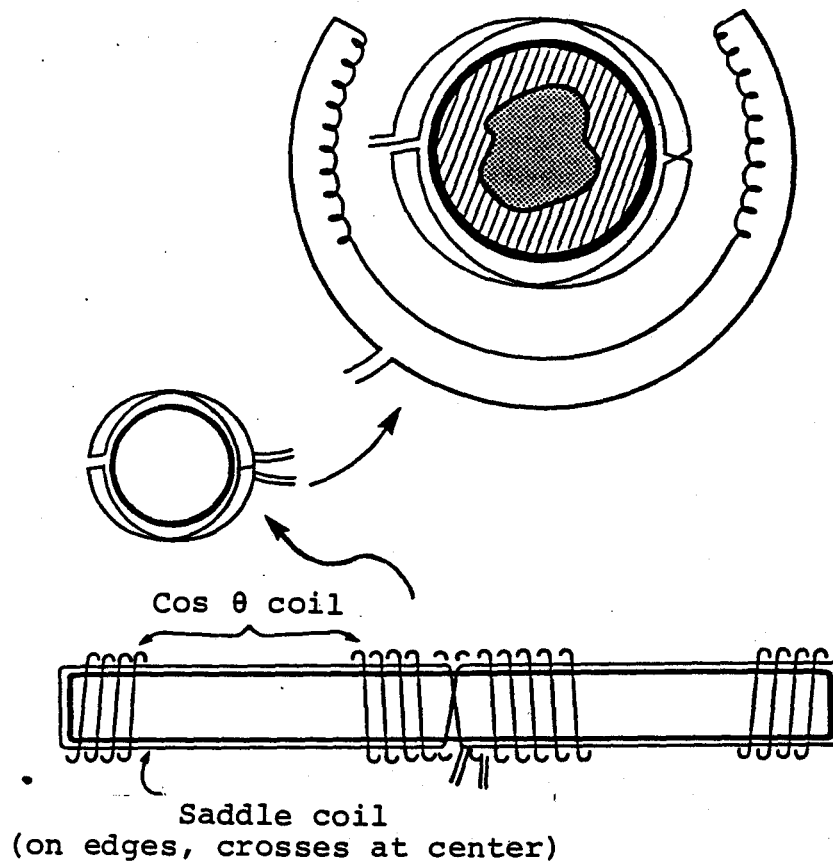


Figure 3.7. The position-sensing pickup coils. The coils are wound on a flat strip which is then bent to encircle the vacuum vessel. The Cos θ coil is wound to approximate a turns density of $n_0 \cos \theta$, while the Saddle coil is wound on the edge.

to keep this field symmetric on either side of the plasma, thus nulling the net $\bar{I}_p \times \bar{B}_v$ force. However, other effects arise due to the finite plasma pressure and toroidal extent; the problem is treated accurately in Section 2.3.

Using B_θ and B_r as given by Mukhovatov[5] (see Equations 2.32 and 2.33), the fluxes linked by each coil may be calculated. For a plasma shifted by some amount relative to the vacuum chamber center, these fluxes are given by the integrals:

$$3.7 \quad \Phi_{\cos} = \int_0^2 \bar{B} \cdot \hat{e} \Big|_{\rho=b} \cos \theta \, d\theta \cdot bN$$

$$3.8 \quad \Phi_{\text{sad}} = 2 \int_0^2 \bar{B} \cdot \hat{\rho} \Big|_{\rho=b} d\theta \cdot bt$$

where ρ = minor radius coordinate from the vacuum chamber center
 θ = similar angle coordinate
 b = radius of pickup coils
 t = width of the coil form = 2.54 cm
 N = peak turns density for the $\cos \theta$ coil times area/turn = 6.5 cm²/cm.

Since the signals appearing at the coil terminals are proportional to $d\Phi/dt$, they are integrated. Arbitrary constants of integration are set equal to zero, and the results are

$$3.9 \quad V_{\text{sad}} = C_s I_p \left[X - \frac{b^2}{2R} \left(\ln \frac{b}{a} + (\Lambda + .5) \left(1 - \frac{a^2}{b^2} \right) \right) \right]$$

$$3.10 \quad V_{\cos} = C_c I_p \left[X + \frac{b^2}{2R} \left(\ln \frac{b}{a} - 1 + (\Lambda + .5) \left(1 + \frac{a^2}{b^2} \right) \right) \right],$$

where X = plasma position
 a = plasma minor radius
 b = pickup coil radius
 R = major radius = .64 m
 I_p = plasma current

and with:

$$C_s I_p = \frac{2 \mu_0 t I_p}{\pi b \tau_s} = .11 \left(\frac{I_p}{100 \text{ kA}} \right) \frac{\text{Volts}}{\text{cm}}$$

$$C_c I_p = \frac{\sqrt{3} \mu_0 N \sigma I_p}{\pi b \tau_c} = .24 \left(\frac{I_p}{100 \text{ kA}} \right) \frac{\text{Volts}}{\text{cm}}$$

where t = coil form width = 2.54 cm
 $\tau_c = \tau_s$ = integrator time constants = .93 ms.

Thus these two signals contain plasma position information from magnetic fields surrounding the plasma. The signals are proportional not only to the position of the plasma, but also to variations in pressure/profile term Λ and minor radius a . A proper linear combination of the saddle and $\cos \theta$ coils can in principle eliminate the Λ dependence, to give a position signal:

$$3.11 \quad V_{c-s} = C_o I_p \left[X - \frac{a^2}{4R} \left(2 \ln \frac{b}{a} + \frac{b^2 - a^2}{a^2} \right) \right].$$

With a gain in the electronics = $K = .7$,

$$C_o = K \frac{4 b t \mu_0}{\pi \tau_s (b^2 + a^2)}$$

results in:

$$3.12 \quad V_{c-s} = .093 (X_{cm} - 1.0 \text{ cm}) \left(\frac{I_p}{100 \text{ kA}} \right) \frac{\text{Volts}}{\text{cm}}$$

for a plasma minor radius of 16 cm. The amplitude of this signal, as well as the offset term (X_o in Equation 3.4, above), still depends on a , the plasma minor radius, but variation in this parameter is assumed to be negligible. This is

accurate within the approximation used in the above calculation, since dV_{c-s}/da is of order a/R with respect to dV_{c-s}/dX (for an approximately centered plasma).

Experimentally, this combination was determined by using the vacuum vertical field to measure the relative magnitudes of the two constants C_c and C_s . The vertical field was pulsed, and the gains of the two signals adjusted to sum to zero. The relative amplitudes of the measured V_{\cos} and V_{sad} signals agreed to within 5% of those calculated for a purely vertical field. The $\cos \theta$ contribution was then reduced by the amount $(b^2 - a^2)/(b^2 + a^2)$ to give the position signal, V_{c-s} in Equation 3.11 above. This is used as the loop error signal.

The constant C_o in Equation 3.11 above was calibrated against other position-sensitive diagnostics, as described in Chapter 4. The agreement with the calculated values is accurate to within the experimental errors of the diagnostics and the numerical calculation of the coefficients.

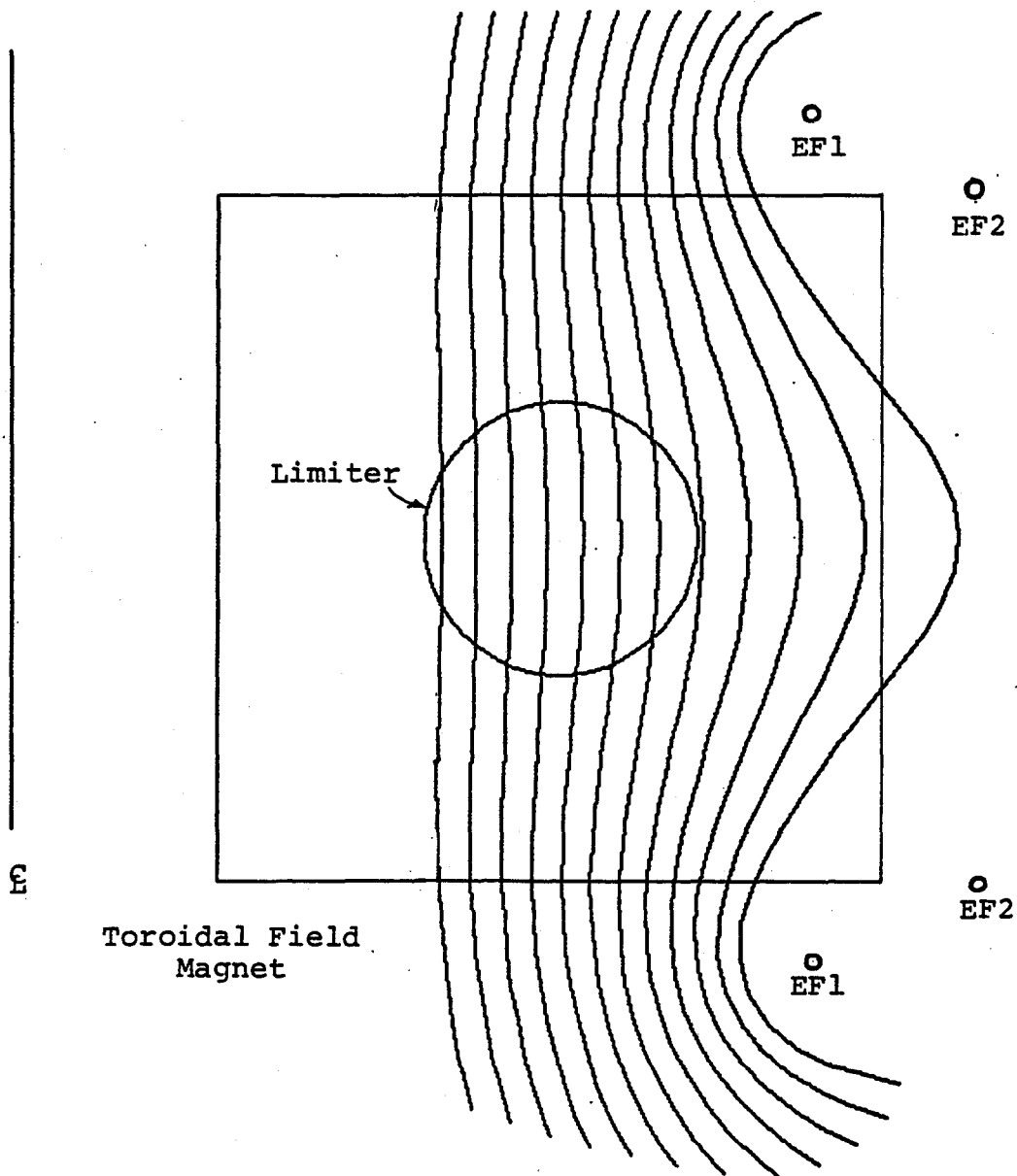


Figure 3.8. The vacuum vertical field. Field lines were generated by plotting surfaces of constant $RA\phi$. The coils are designated by EF1 and EF2.

of the physical model; inward equilibrium forces generated by $\bar{I}_p \times \bar{B}_v$ counteract the plasma tendency to expand). However, the plasma is a conducting ring that, in order to expand, must cut more vertical field flux. From conservation of magnetic field energy this arrangement can be stable, but sets an upper limit on the decay of the field: n must be less than $3/2$. These conditions, $0 < n < 3/2$, are met by the vacuum vertical field. In Appendix III, the vertical field strength and vertical field index are listed for various positions in the vacuum chamber. The field values were calculated by numerically differentiating the potential from Equation 3.13, above.

Since the vertical field is not strictly homogeneous across the area of the vacuum chamber, several poloidal field harmonics are present. Further, various stray fields occur within the plasma chamber. Affecting the vertical field index, as well as the equilibrium shape of the plasma, these fields are described in Section 3.4.

3.3.2 Time Delays Associated with the Vertical Field

The vertical field must pass through the Bitter plates of the toroidal field coil, and also through the vacuum chamber walls. Since these are conductors, penetration delays can result. As measurements and calculations show, however, these delays take place on time scales of .1-.2 ms, and are assumed to be insignificant to the dynamics of the system (see Appendix II for the experimental measurements).

3.4 Stray Fields Affecting the Plasma

There are several fields with vertical components in the region of the vacuum chamber. The toroidal field winding has a net single turn due to its helicity: the turn-to-turn crossovers are equivalent to a loop carrying the toroidal field current. They occur inside the major radius of the plasma, and have roughly rectangular cross sections. To a good approximation, this single turn results in a stray vertical field of approximately 150 Gauss in the center and 250 Gauss at the inside edge of the plasma, for a toroidal field current of 100 kA. By comparison, a 400 kA plasma discharge has a poloidal field of 5 kG, with an imposed equilibrium vertical field of 1.8 kG. (There is also a stray horizontal field component due to a vertical displacement of the single turn. This varies, but is usually about 30 Gauss.)

Since a field null is necessary to achieve the electron avalanche necessary for the initial breakdown, a compensating bias field must be applied to cancel these stray components. The stray toroidal field, the bias field, and their sum are shown in Figure 3.9. (Only the vertical fields are illustrated.) Since the bias field has a different decay index from the single turn field, they can only be nulled at one point, but this is sufficient for initiation of the plasma. For this operation, the breakdown has in fact been observed to originate at the outside of the major radius of the vacuum chamber [3], which is consistent with the expected field null position.

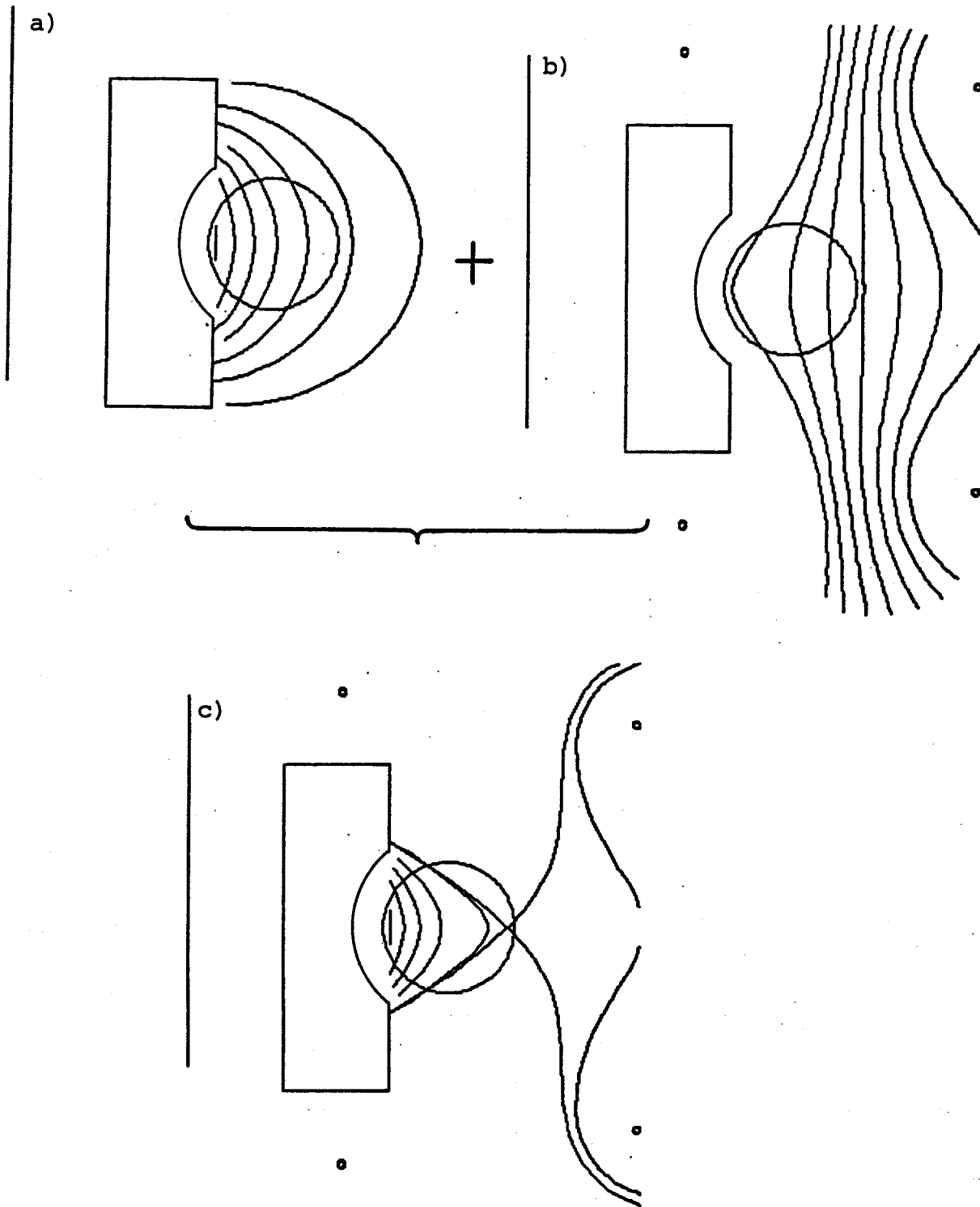


Figure 3.9. The stray component of the toroidal field, as nulled by the bias field. a) the stray toroidal field. b) the bias field. c) their sum; a field null occurs near the outside edge of the vacuum chamber.

The vertical field index, as given by formula 3.14 and in Appendix III, is changed when these stray fields are included. Theoretically, the index is now such that the plasma is not always stable to in-out perturbations, as described in Section 3.3. This is particularly true during the current rise and fall, when the stray fields are of the same order as the applied equilibrium field. Experimentally, however, this does not seem to be important. The position appears to be stable to this mode at all times during the discharge, except possibly the last 10 ms. During this time, the plasma current is ramping down, but the discharge almost always terminates before the current reaches zero. This termination is accompanied by large position excursions, indicating a possibly unstable index situation. Appendix III contains values of the index for each vacuum field present that may be applied to the plasma, and explains the method for calculating the total index for a given set of currents.

Chapter 4. Performance and Results

4.1 Performance.

Data from a typical Alcator C plasma discharge is shown in Figure 4.1. Signals from the plasma current, Cos-Saddle position loops, central density, and central soft X-ray emission, are shown. The actual position of the plasma is computed from the Cos-Sad signal according to Equation 3.12, and is also plotted. The Cos-Sad signal is the loop error Voltage, and is explained in detail in Chapter 3. The plasma density is measured with an infrared laser interferometer on five chords through the plasma. For the central chord shown in the figure, each interference fringe represents $.58 \times 10^{14}$ electrons per cm^3 ; other chords are located at -12 cm, -6 cm, +8.5 cm, and +15 cm. With distances referenced to the center of the vacuum vessel, positive = greater major radius. Soft X-ray emission is measured at chords spaced every 2 cm, from -12 cm to +14 cm. The measured X-ray signal has a complicated dependence on a number of factors, among them plasma temperature, density, and level of impurities, so the absolute magnitude of this signal is not easily interpretable.

The plasma discharge of Figure 4.1 is typical for Alcator position feedback operation. There is a small error in the initial vertical field, causing an excursion in the position before the control circuit has time to respond. During the subsequent 60 ms of the discharge, the plasma current and beta are rapidly increasing, and also the profile is changing.

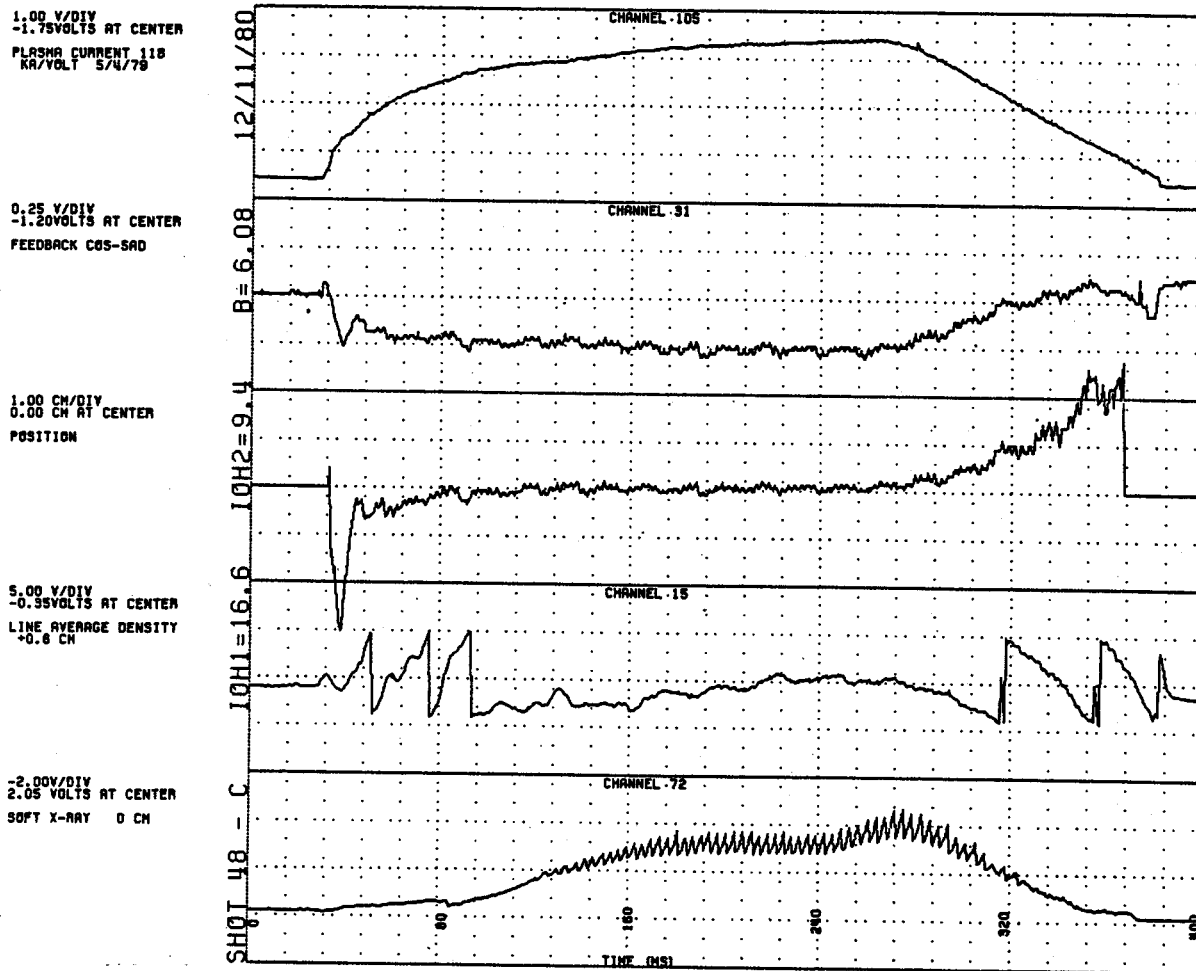


Figure 4.1. A typical Alcator C plasma discharge. The position signal is calculated from the Cos-Sad data divided by the current, according to equation 3.12.

This results in a larger error signal than during the period from 80 to 270 ms, and thus poorer position. Similarly, as the plasma current is decreased at the end of the discharge, the beta and internal inductance are again changing, also resulting in a larger error signal.

The position response to a programmed step is shown in Figure 4.2. (Note: The step had a 3.6 ms time constant on its rising and falling edges.) Plasma current and soft X-ray emission are shown, along with vertical field current. The net plasma motion is about 2 cm. As the center moves, the central X-ray signal changes due to the motion of the peak emitting region of the plasma; immediately following the step, the soft X-ray signals from all detectors increase, indicating an influx of impurities from the wall or limiter. This shot was produced with the normal settings of the feedback gain and lead adjustment, and illustrates the good control and lack of overshoot available from the closed loop system.

In normal operation, the feedback system has good stability. Typical response is free from overshoot, as in each of the cases presented herein. This is consistent with the analysis of Section 3.1.3, in which the average time of 1.4 ms was used for the delay of the SCR supply.

In Figure 4.3, two disruptive plasma shots are shown. A plasma disruption is characterized by abrupt changes in current, temperature and density profiles (on a time scale of 100 μ s), and represents an step-like disturbance to the plasma equilibrium. In each case, the feedback system restores the

1.00 V/DIV
-1.85VOLTS AT CENTER
PLASMA CURRENT 118
KA/VOLT 5/4/78

-1.00V/DIV
3.25 VOLTS AT CENTER
SOFT X-RAY 0 CH

1.00 V/DIV
1.80 VOLTS AT CENTER
VERTICAL FIELD
CURRENT = .000487 A

0.25 V/DIV
-0.90VOLTS AT CENTER
FEEDBACK COS-SAD
= (X-1)MIP/(I.INR)

1.00 CM/DIV
0.00 CM AT CENTER
POSITION

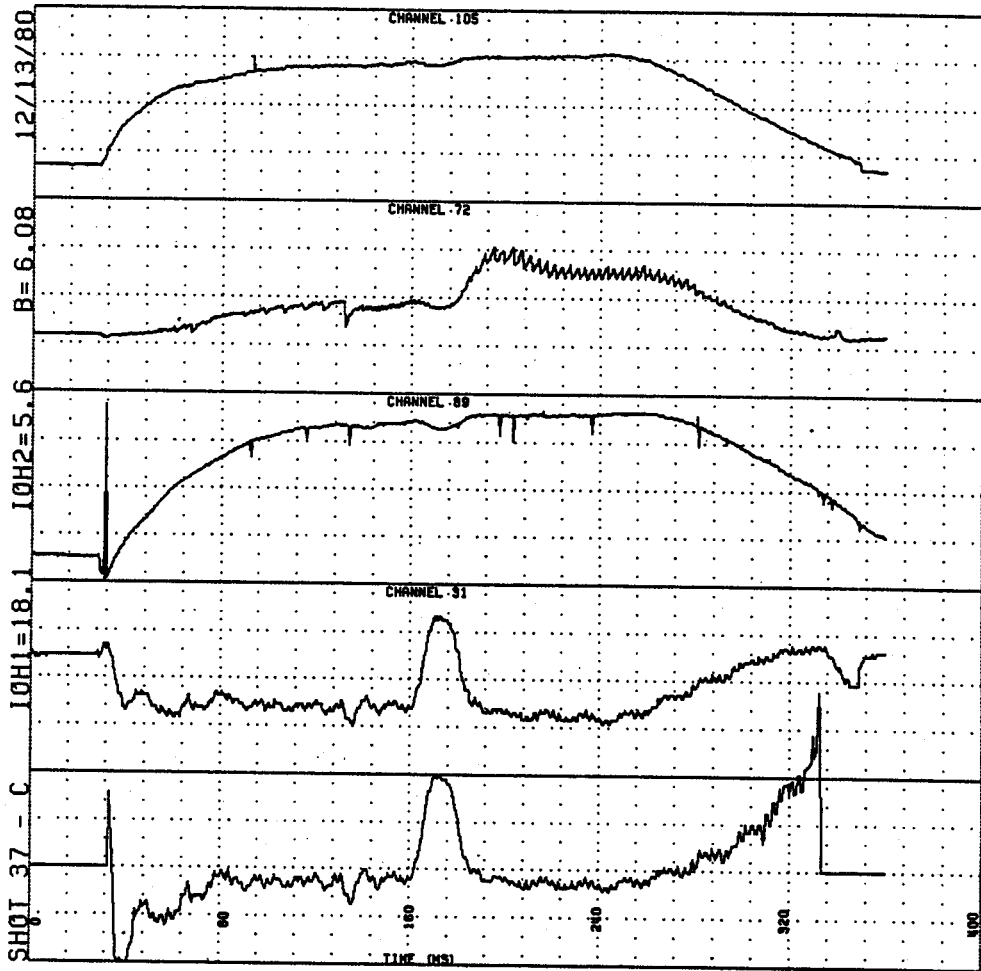


Figure 4.2. The plasma response to a programmed step in position. (Note: the step had a 3.6 ms rise and fall time.)

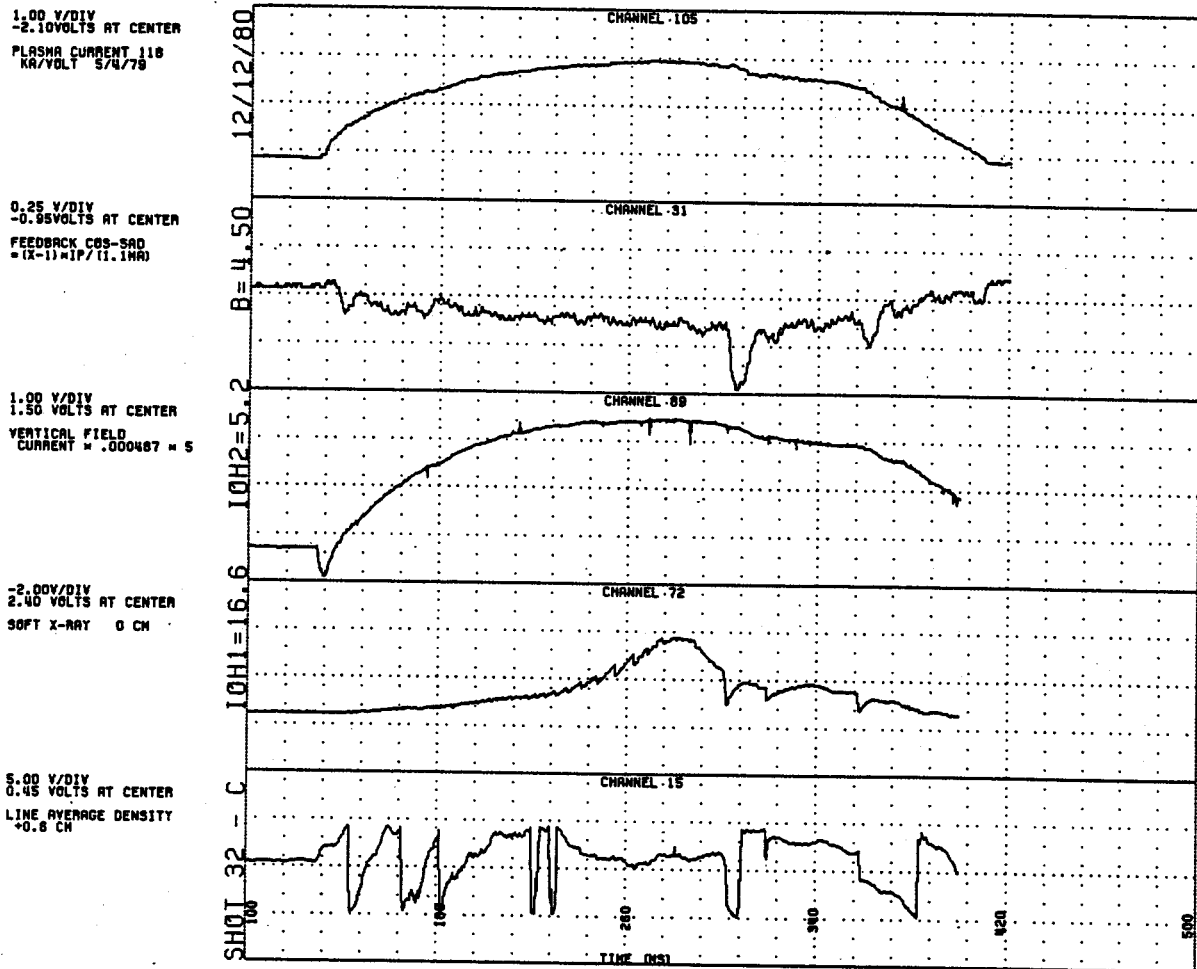


Figure 4.3a. Minor disruption of the plasma (at $t = 300$ ms). During a disruption, the plasma equilibrium changes on a time scale of $100 \mu\text{s}$, requiring adjustment of the vertical field current to restore the position.

1.00 V/DIV
5.25 VOLTS AT CENTER
PLASMA CURRENT
118 KA/VOLT

0.25 V/DIV
-1.10VOLTS AT CENTER
FEEDBACK CBS-SAD
= (X-1) * IP / (1.1RA)

1.00 V/DIV
1.85 VOLTS AT CENTER
VERTICAL FIELD
CURRENT = .000487 A S

-2.00V/DIV
3.45 VOLTS AT CENTER
SOFT X-RAY 0 CM

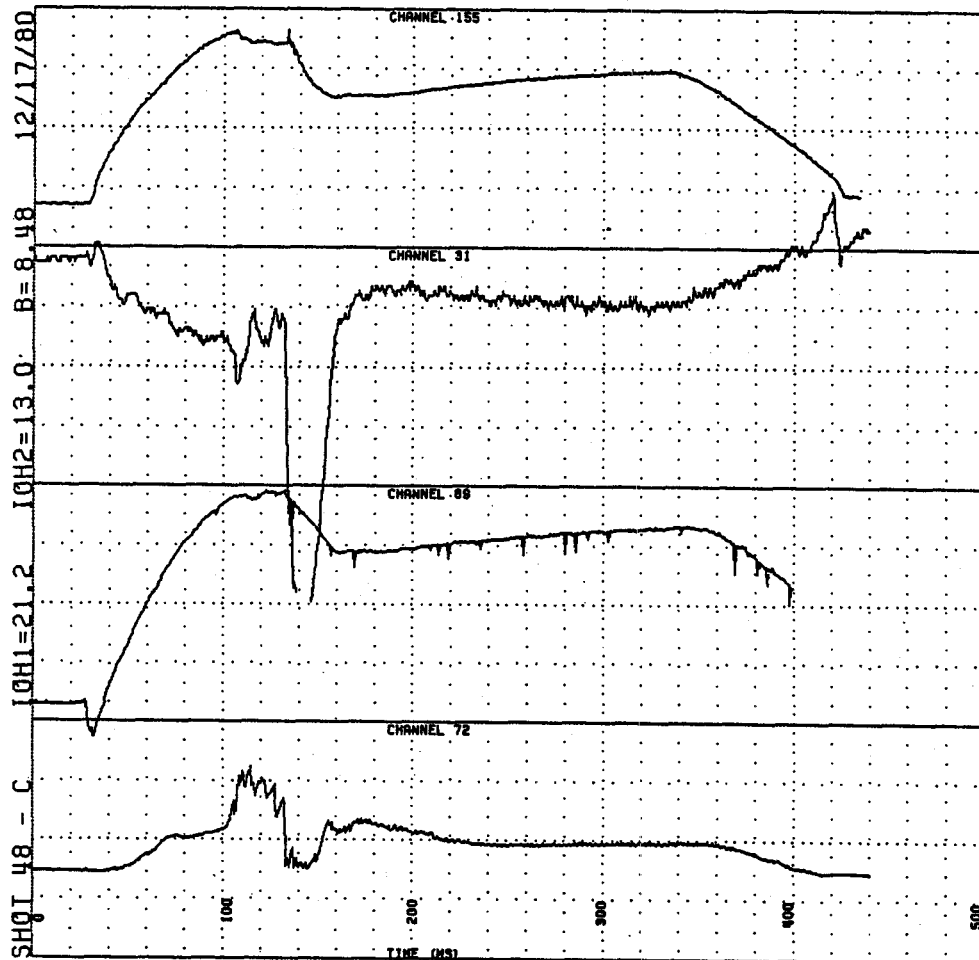


Figure 4.3b. A somewhat larger disruption. The position recovery time is limited by the SCR output current slew rate.

position of the plasma within a short time. In the second shot, the plasma discharge was severely damaged before the position was restored; the speed of recovery was limited by the output current slew rate of the vertical field SCR supply.

That the linear analysis of the stability of the feedback circuit is approximately correct is further established by operation of the feedback system with an unstable closed loop response. According to Bode plots of open loop gain and phase (see Chapter 3), setting the lead = 0 should result in an unstable situation. Experimentally, the position is indeed unstable; such a case is shown in Figure 4.4. The premature plasma termination is probably due to the introduction of impurities. A second region of instability should occur for an open loop DC gain which is 20% higher than the normal setting, and this is also observed. In this case, the oscillation seems to lock to a subharmonic of the line frequency, a nonlinear effect that is probably due to the three-phase delay, and is not considered in the preceding analysis. Operation in this regime is shown in Figure 4.5.

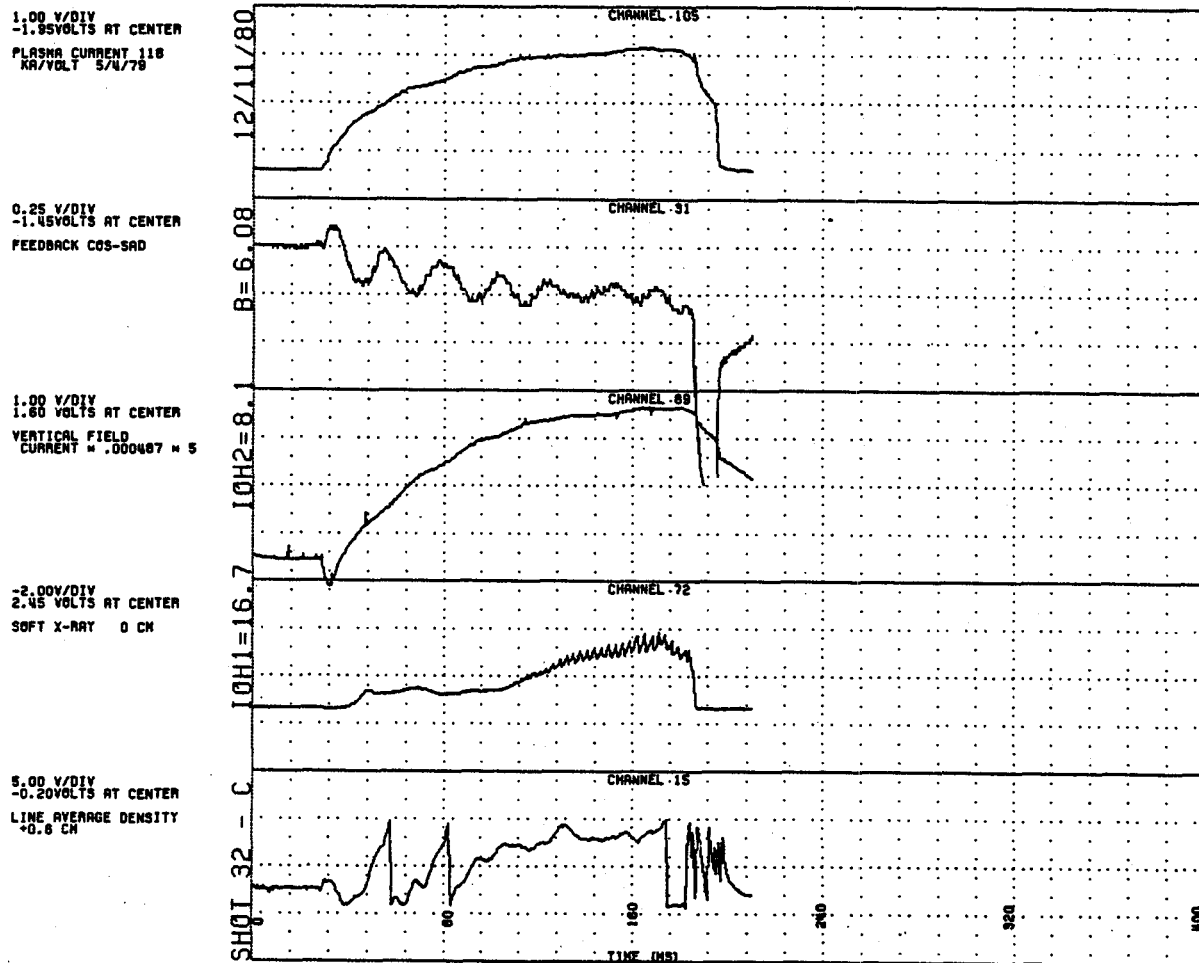


Figure 4.4. Unstable operation of the feedback system (no lead). The oscillation amplitude is limited by the slew rate of the vertical field current.

1.00 V/DIV
-1.70VOLTS AT CENTER
PLASMA CURRENT 118
KA/VOLT 5/4/78

0.25 V/DIV
-1.15VOLTS AT CENTER
FEEDBACK CGS-9AD

1.00 V/DIV
1.85 VOLTS AT CENTER
VERTICAL FIELD
CURRENT = .000487 A

-2.00V/DIV
2.35 VOLTS AT CENTER
SOFT X-RAY 0 CH

5.00 V/DIV
0.35 VOLTS AT CENTER
LINE AVERAGE DENSITY
+0.8 CH

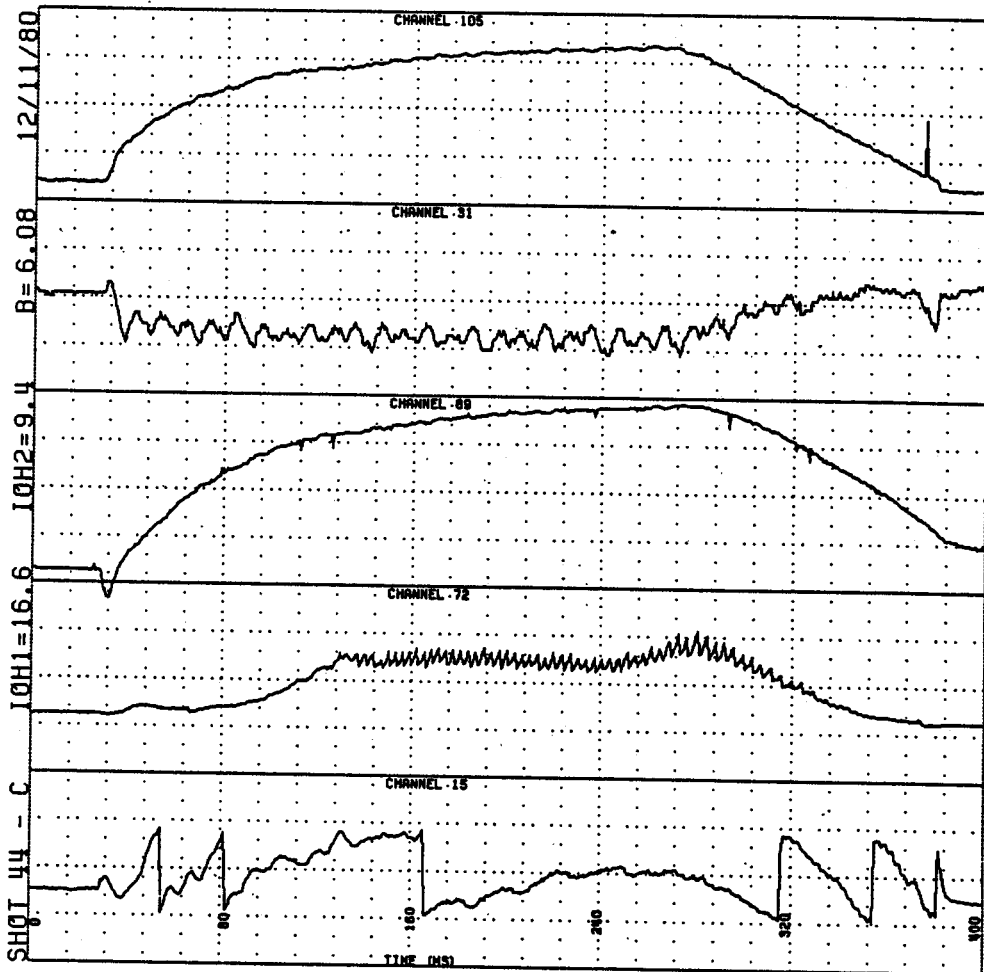


Figure 4.5. Unstable operation of the feedback system (too much gain). The oscillation appears to cause a non-linear interaction in the SCR supply between the "rising" and "falling" input responses and the three phase delay.

4.2 Results

There are a number of position-sensitive diagnostics available for comparison with the pickup loop signals. A step was programmed for the plasma position in the discharge shown in Figure 4.6. Centroids of the density and soft X-ray profiles are computed, and their locations are shown as functions of time. Also shown is the position of the outermost flux surface as indicated by the Cos-Saddle signal (which is divided by plasma current and offset 1 cm, according to Equation 3.12). The relative changes in position measured by each diagnostic agree with each other to better than 10%, which is the approximate experimental error of the data.

The soft X-ray centroid position is offset from the flux surface and density measurements by about 2 cm, indicating a shift of the hottest part of the plasma towards the outside. This is the only evidence of the Shafranov shift that was described in Chapter 2. The density centroid is not offset, and profiles are virtually always symmetric about their centers (see Figure 2.6). This is in contrast to the expected density profiles for a plasma with shifted inner flux surfaces, also shown in Figure 2.6.

Electron cyclotron harmonic emission is used to measure electron temperature profiles, and is a third diagnostic sensitive to position. A typical electron cyclotron profile is shown in Figure 2.1. The position of the center of the fitted profile depends on the exact magnitude of the toroidal field, so it is not possible to determine the absolute

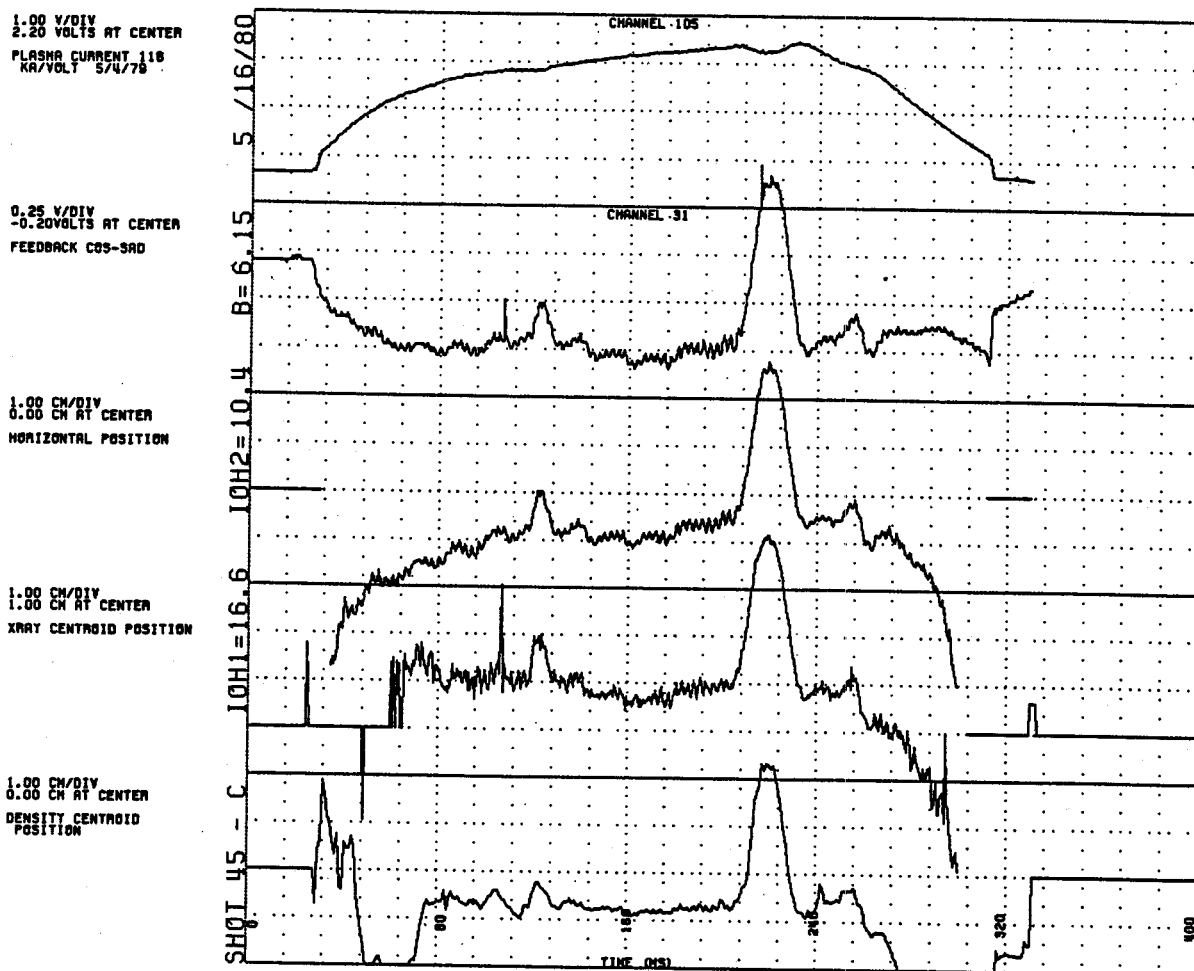


Figure 4.6. Comparison of position-sensitive diagnostics with the flux surface measurement. The shift of the soft X-ray signal to the outside is evidence of the Shafranov shift. (Note that the center of this trace is at 1 cm.)

location of the plasma center with accuracy of greater than about ± 2 cm. However, relative changes in the positions of these profiles agree well with those measured by the diagnostics discussed above. Figure 4.7 shows electron cyclotron-measured positions plotted against those taken from the flux loops; the least squares fit to the data has a slope of about .9. The shift of the data to 1 cm outside may not be taken as evidence of a Shafranov shift, due to the aforementioned errors.

If the peak of the temperature Gaussian is arbitrarily made to coincide with the peak of the X-ray signals, constant pressure surfaces may be computed using experimental density profiles. These are indeed shifted at the center with respect to the outermost, but the net shift is only about one third to one half of the expected Shafranov shift. To produce the proper amount of shift, a small temperature offset, varying linearly with major radius, must be added to the Gaussian profile of the temperature. The offset needed is about +7% of the peak at the smallest major radius of the discharge, varying to -7% at the outermost. Such a perturbation is probably below the limits of the resolution of the diagnostic.

Thermocouples mounted on the limiter are used to measure heating its heating at various locations poloidally. Factors besides poor positioning affect the heating of the limiter, but centering the plasma according to the above diagnostics qualitatively seems to maximize the uniformity of the thermal loading. For plasma discharges whose average position varied

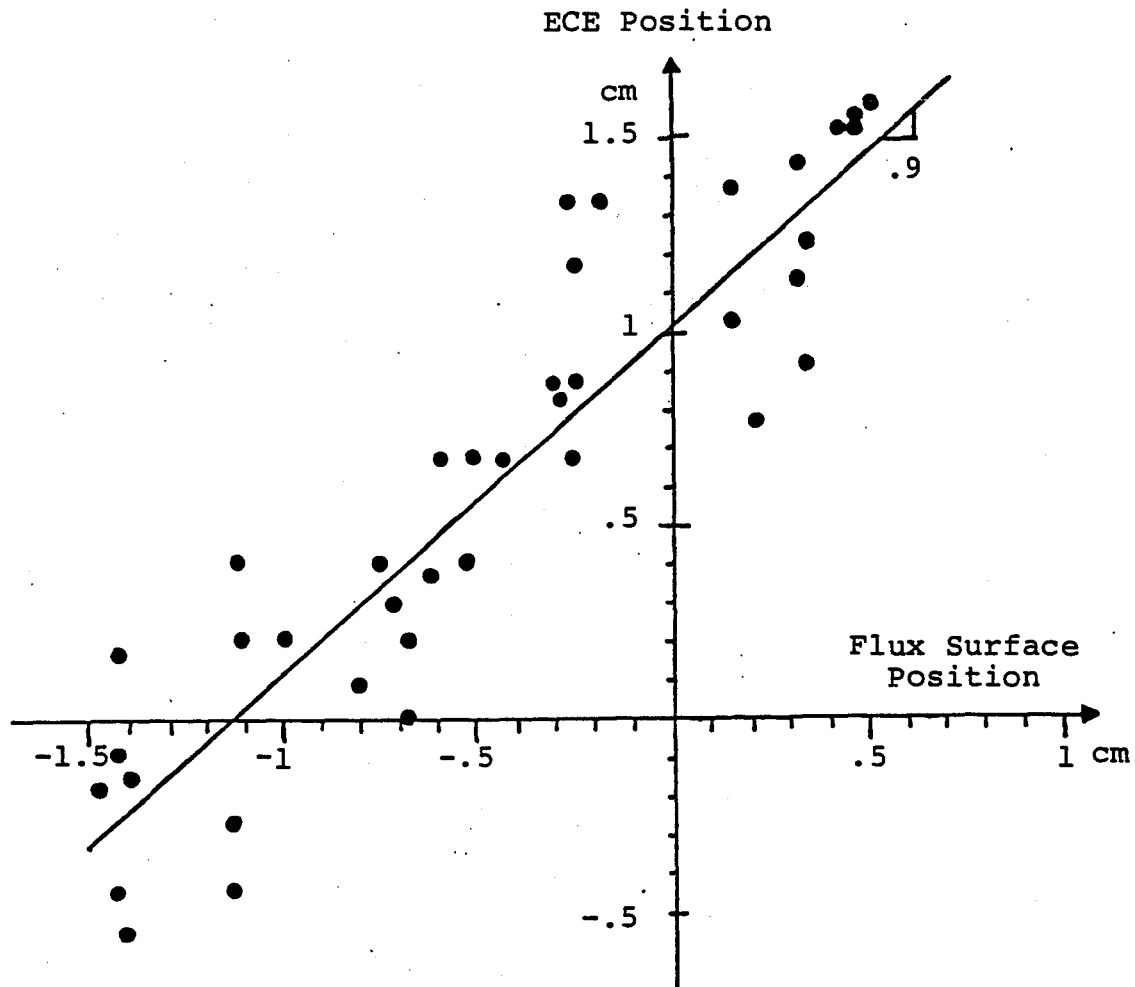


Figure 4.7. Positions measured by Electron Cyclotron Emission, plotted against measured flux surface position. Errors in absolute position are ± 2 cm, so the above shift is not evidence of the Shafranov shift.

from -1 cm to +1 cm, the differential limiter heating is plotted in Figure 4.8. The vertical axis is the difference between the quantities of heat received on the inner- and outer-120 degree sections of the limiter, divided by the total energy received by both; the horizontal axis is the average position as measured by the flux loops. In general, centering results in the most even heating, though there may be large fluctuations from shot to shot.

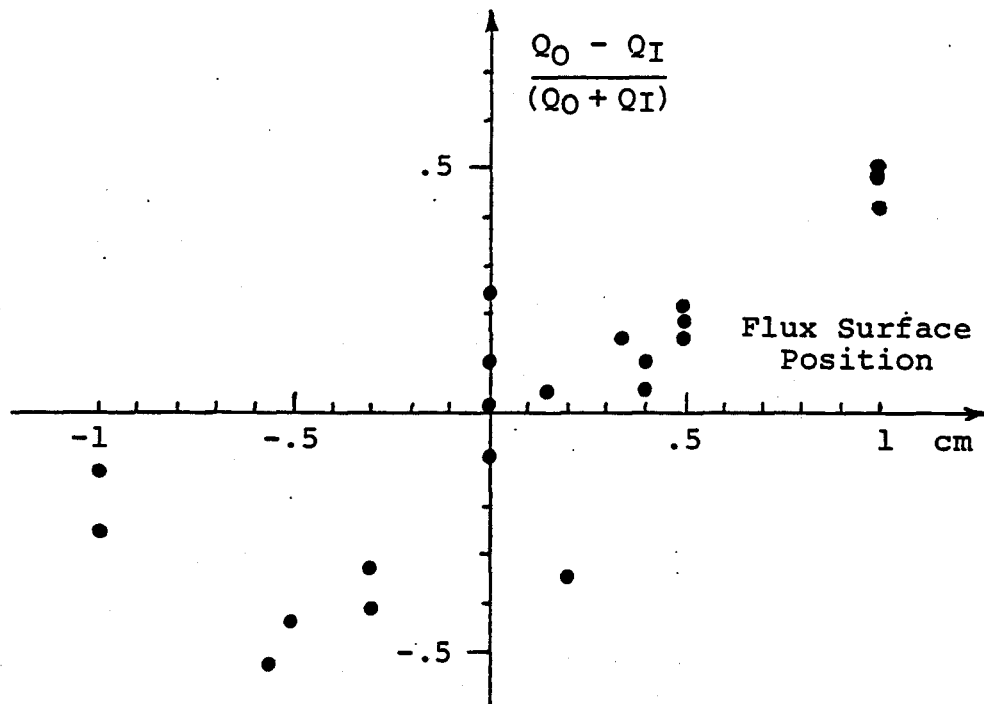


Figure 4.8 Differential limiter heating vs. the average position of the outer flux surface. The vertical axis is the difference in heat energy received by the outer and inner segments, divided by the total. In general, centering the plasma results in the most even thermal loading of the limiter.

Note on determination of soft X-ray profiles:

Because of the geometry, and individual variations in diode sensitivity and window thickness, determination of soft X-ray profiles is somewhat arbitrary. In this work, two means were used: 1) As the plasma is moved in a step, the detector closest to the peak of the emission profile will change the least. This can be used to determine the center of the profile, and the amplitudes of symmetric detectors can then be adjusted to give symmetric profiles. Further, an assumption is made that as the plasma is moved initially by 2 cm, the emission profile is of approximately constant shape and magnitude; this results in each detector's seeing the plasma chord which the immediately inside neighbor previously viewed, and the gains can be adjusted accordingly. 2) The center of the plasma normally undergoes a relaxation oscillation denoted by "saw-teeth" in the hottest part of the plasma, and if they are assumed to be symmetric about the peak, can give an independent calibration of the location of the peak of the emission profile.

Chapter 5. Conclusions

Position control of the Alcator C plasma has been implemented. The feedback system typically operates with good stability and little overshoot, and enables the plasma discharge to recover from minor disruptions with little harm. This feedback control system is in daily use for the Alcator C runs.

At the date of this writing, a similar control system has been developed for control of the up-down plasma position. This is still in the prototype stage, but is also used in daily operation.

With plasma diagnostics currently available, the existence of the Shafranov shift may neither be conclusively proven nor disproven. The soft X-ray signals seem to indicate that the hottest region of the plasma is displaced with respect to the outermost flux surface, but temperature and density profiles are not able to resolve the concomitant asymmetries in the pressure profile.

The influence of the shape of the plasma on the various position-sensitive diagnostics was also investigated. Theoretically, the perturbations to circularity affect temperature and density profiles even less than the Shafranov shift; thus they are apparently not measurable. However, the lack of measurements of the Shafranov shift is also not attributable to any plasma shape effect.

Relative changes in the measured position of the outermost flux surface are demonstrated to be in good agreement

with other position-sensitive diagnostics. Soft X-ray, density, and temperature profiles all agree with the flux loop measurement to within their experimental errors. Further, the thermal loading of the limiter is most even for discharges that are centered according to the flux loops.

More work will be required to establish the existence of the Shafranov shift. Also, limiter heating and poloidally resolved flux loop measurements may be used to experimentally investigate the shape of the plasma. This must be undertaken in order to do a more advanced comparison of the predicted versus observed MHD equilibria.

Appendix I. A Derivation of the Grad Shafranov Equation

The MHD equations used for the derivation of the Grad-Shafranov equation are:

$$2.1 \quad \nabla \cdot \bar{B} = 0$$

$$2.2 \quad \nabla \times B = \mu_0 J$$

$$2.3 \quad \bar{J} \times \bar{B} = \nabla p.$$

For this model, all dissipation effects are neglected, and plasma conductivity is assumed to be infinite. No variation along \hat{e}_ϕ is assumed, so $\partial/\partial\phi = 0$. Pressure p is assumed to be a scalar. This derivation is originally credited to J. Freidberg [1].

Beginning in cylindrical coordinates, B can be expressed

$$\begin{aligned} 2.4 \quad \bar{B} &= \frac{1}{R} \nabla \psi \times \hat{e}_\phi + B_\phi \hat{e}_\phi \\ &= \hat{e}_R \frac{-1}{R} \frac{\partial \psi}{\partial z} + \hat{e}_\phi B_\phi + \hat{e}_z \frac{1}{R} \frac{\partial \psi}{\partial R}, \end{aligned}$$

which is equivalent to 2.1, $\nabla \cdot \bar{B} = 0$. Equation 2.4a of Chapter 2 is derived only after the change of coordinates at the end of this appendix. Taking the curl of the above expression for \bar{B} ,

$$\mu_0 \bar{J} = \nabla \times \bar{B} = -\hat{e}_R \frac{\partial B_\phi}{\partial z} - \hat{e}_\phi \left(\frac{1}{R} \frac{\partial^2 \psi}{\partial z^2} + \frac{\partial}{\partial R} \frac{1}{R} \frac{\partial \psi}{\partial R} \right) + \hat{e}_z \frac{1}{R} \frac{\partial}{\partial R} (R B_\phi).$$

Defining the operator Δ^* , this becomes

$$2.5 \quad \mu_0 \bar{J} = -\frac{1}{R} \Delta^* \psi \hat{e}_\phi + \frac{1}{R} \nabla (R B_\phi) \times \hat{e}_\phi$$

with

$$\Delta^* \psi = R \frac{\partial}{\partial R} \frac{1}{R} \frac{\partial \psi}{\partial R} + \frac{\partial^2 \psi}{\partial z^2}.$$

Next, Freidberg notes that since $\bar{\mathbf{B}} \cdot \bar{\mathbf{J}} \times \bar{\mathbf{B}} = 0$, Equation 2.3 results in $\bar{\mathbf{B}} \cdot \nabla p = 0$, also. This implies that $p = p(\psi)$, since $\partial/\partial\phi = 0$ and B_R and B_z are only functions of ψ . With this in mind, ∇p becomes $\nabla\psi (dp/d\psi)$ in the following equations. Similarly, $\bar{\mathbf{J}} \cdot \bar{\mathbf{J}} \times \bar{\mathbf{B}} = 0$ results in

$$0 = \mu_0 \bar{\mathbf{J}} \cdot \nabla p$$

$$0 = \left[\frac{1}{R} \nabla(RB_\phi) \times \hat{\mathbf{e}}_\phi \right] \cdot \nabla\psi \frac{dp}{d\psi}$$

when the expression in Equation 2.5 is used for $\bar{\mathbf{J}}$. This implies that RB_ϕ is also only a function of ψ . The function F is defined:

$$2.6 \quad F(\psi) \equiv RB_\phi$$

with

$$\nabla F = \frac{dF}{d\psi} \nabla\psi.$$

Substitution of these expressions for $\bar{\mathbf{B}}$ and $\bar{\mathbf{J}}$ into Equation 2.3 results in the Grad-Shafranov equation. That is,

$$\mu_0 \bar{\mathbf{J}} \times \bar{\mathbf{B}} = \mu_0 \nabla p$$

$$\left[-\frac{1}{R} \Delta^* \psi \hat{\mathbf{e}}_\phi + \frac{1}{R} \nabla F \times \hat{\mathbf{e}}_\phi \right] \times \left[B_\phi \hat{\mathbf{e}}_\phi + \frac{1}{R} \nabla\psi \times \hat{\mathbf{e}}_\phi \right] = \mu_0 \nabla p$$

$$\frac{-1}{R^2} \Delta^* \psi \hat{\mathbf{e}}_\phi \times (\nabla\psi \times \hat{\mathbf{e}}_\phi) + \frac{1}{R^2} F (\nabla F \times \hat{\mathbf{e}}_\phi) \times \hat{\mathbf{e}}_\phi = \mu_0 \nabla p$$

$$- \Delta^* \psi \hat{\mathbf{e}}_\phi \times (\nabla\psi \times \hat{\mathbf{e}}_\phi) = \mu_0 R^2 \frac{dp}{d\psi} \nabla\psi + F \frac{dF}{d\psi} \hat{\mathbf{e}}_\phi \times (\nabla\psi \times \hat{\mathbf{e}}_\phi),$$

and since $\nabla\psi$ is perpendicular to $\hat{\mathbf{e}}_\phi$,

$$2.7 \quad - \Delta^* \psi = \mu_0 R^2 \frac{dp}{d\psi} + F \frac{dF}{d\psi},$$

which is the desired result.

For a tokamak, it is necessary to convert from the cylindrical geometry used in the derivation so far to a toroidal coordinate system. Figure A.I.1 shows the toroidal coordinates used: r , θ , ϕ , and with major radius R_0 . It is apparent that

$$R = R_0 + r \cos \theta$$

$$z = r \sin \theta$$

$$\phi = \phi .$$

The operator Δ^* is converted to toroidal coordinates by expressing the derivatives

$$\frac{\partial Q}{\partial R} = \frac{\partial Q}{\partial r} \frac{dr}{dR} + \frac{\partial Q}{\partial \theta} \frac{d\theta}{dR}$$

$$\frac{\partial Q}{\partial z} = \frac{\partial Q}{\partial r} \frac{dr}{dz} + \frac{\partial Q}{\partial \theta} \frac{d\theta}{dz} .$$

The derivatives dr/dR and dz/dR are calculated from the expression $r^2 = z^2 + (R-R_0)^2$, and the above relations between the coordinates:

$$\frac{dr}{dR} = \frac{R - R_0}{r} = \cos \theta$$

$$\frac{dr}{dz} = \frac{z}{r} = \sin \theta .$$

The remaining $d\theta/dR$ and $d\theta/dz$ terms may be calculated by differentiating $z = r \sin \theta$:

$$0 = \frac{dr}{dR} \sin \theta + r \cos \theta \frac{d\theta}{dR}$$

$$\frac{d\theta}{dR} = - \frac{\sin \theta}{r} ,$$

and also:

$$1 = \frac{dr}{dz} \sin \theta + r \cos \theta \frac{d\theta}{dz}$$

$$\frac{d\theta}{dz} = \frac{\cos \theta}{r} .$$

Algebra then leads to the expression for Δ^* in toroidal coordinates:

$$2.8 \quad \Delta^* \psi = \frac{1}{r} \frac{\partial}{\partial r} r \frac{\partial \psi}{\partial r} + \frac{1}{r^2} \frac{\partial^2 \psi}{\partial \theta^2} - \frac{1}{R} \left(\frac{\partial \psi}{\partial r} \cos \theta - \frac{\sin \theta}{r} \frac{\partial \psi}{\partial \theta} \right).$$

Further, Equation 2.4a may now be established:

$$B_p = \frac{1}{R} \psi \times \hat{e}_\theta$$

$$= \hat{e}_R \left(-\frac{1}{R} \frac{\partial \psi}{\partial z} \right) + \hat{e}_z \frac{1}{R} \frac{\partial \psi}{\partial R}$$

$$= (\hat{e}_r \cos \theta - \hat{e}_\theta \sin \theta) \left(-\frac{1}{R} \frac{\partial \psi}{\partial r} \sin \theta - \frac{1}{R} \frac{\partial \psi}{\partial \theta} \frac{\cos \theta}{r} \right)$$

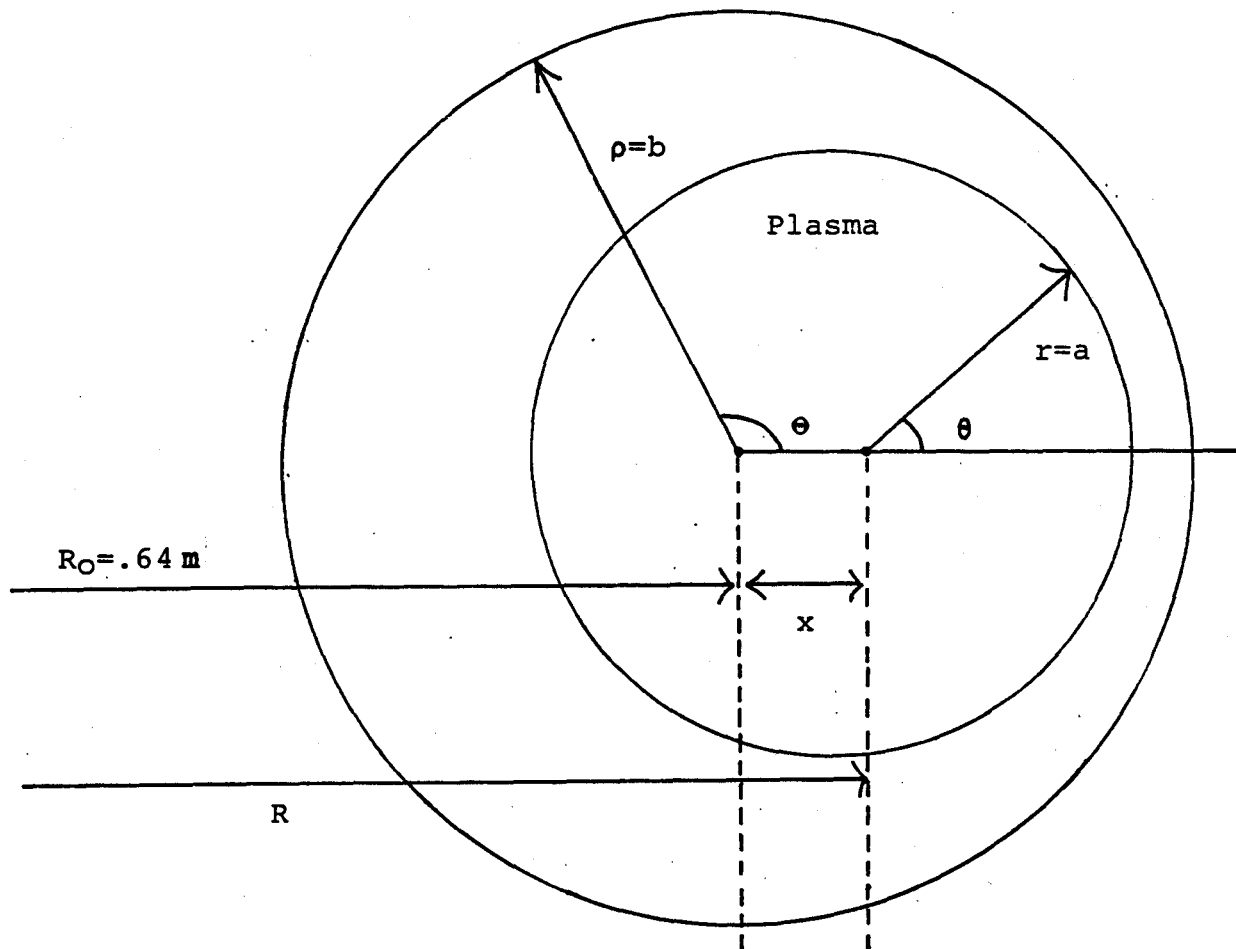
$$+ (\hat{e}_r \sin \theta + \hat{e}_\theta \cos \theta) \left(\frac{1}{R} \frac{\partial \psi}{\partial r} \cos \theta - \frac{1}{R} \frac{\partial \psi}{\partial \theta} \frac{\sin \theta}{r} \right).$$

In the \hat{e}_θ direction, this is equivalently:

$$2.4a \quad B_\theta = \frac{1}{R} \frac{\partial \psi}{\partial r} .$$

In addition, the expression for the field in the \hat{e}_r direction is:

$$B_r = -\frac{1}{R} \frac{1}{r} \frac{\partial \psi}{\partial \theta} .$$



Coordinates

R = major radius of plasma

r = minor radius of plasma

θ = azimuthal angle of plasma

ρ = minor radius with respect to vacuum chamber center

θ' = similar angle

x = displacement of plasma center from vacuum chamber center

Figure A.II.1. The toroidal coordinate system.

Appendix II. Delays Due to the Vertical Field Penetration of the Tokamak Structure

A.II.1 Penetration of the Vertical Field through the Toroidal Field Magnet

The Alcator C toroidal field magnet is of Bitter plate construction. That is, individual copper plates are cut and formed together to create a square helix around the vacuum chamber (see Figure A.II.1). There is also a helical insulator between the plates, and this laminated construction permits vertical fields to pass relatively unimpeded. Eddy currents can flow in the plates, but the average vertical field in the center can be shown to be the same as the average applied vertical field. Since the actual geometry is complicated, however, two limiting cases will be considered.

A.II.1.1 Case 1

Infinitely wide parallel plates are considered, with field applied perpendicular to their ends (see Figure A.II.2). Solving Maxwell's equations and matching boundary conditions at the ends of the plates:

$$B = B_n \cos\left(\frac{n\pi x}{L}\right) \exp\left(\frac{-n\pi z}{L}\right).$$

By symmetry, or since $\nabla \cdot B = 0$, the space average field on both ends of the plates must be the same. Solution of Laplace's equation shows that, at a distance equal to a plate's-width from the ends, even the first harmonic is attenuated by $e^{-2\pi}$.

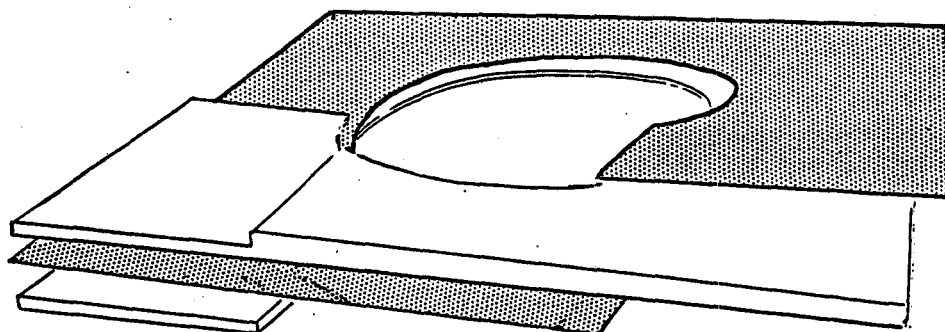


Figure A.II.1. The toroidal field Bitter plate construction. The plates are interleaved with an insulator, and form a helix around the vacuum chamber.

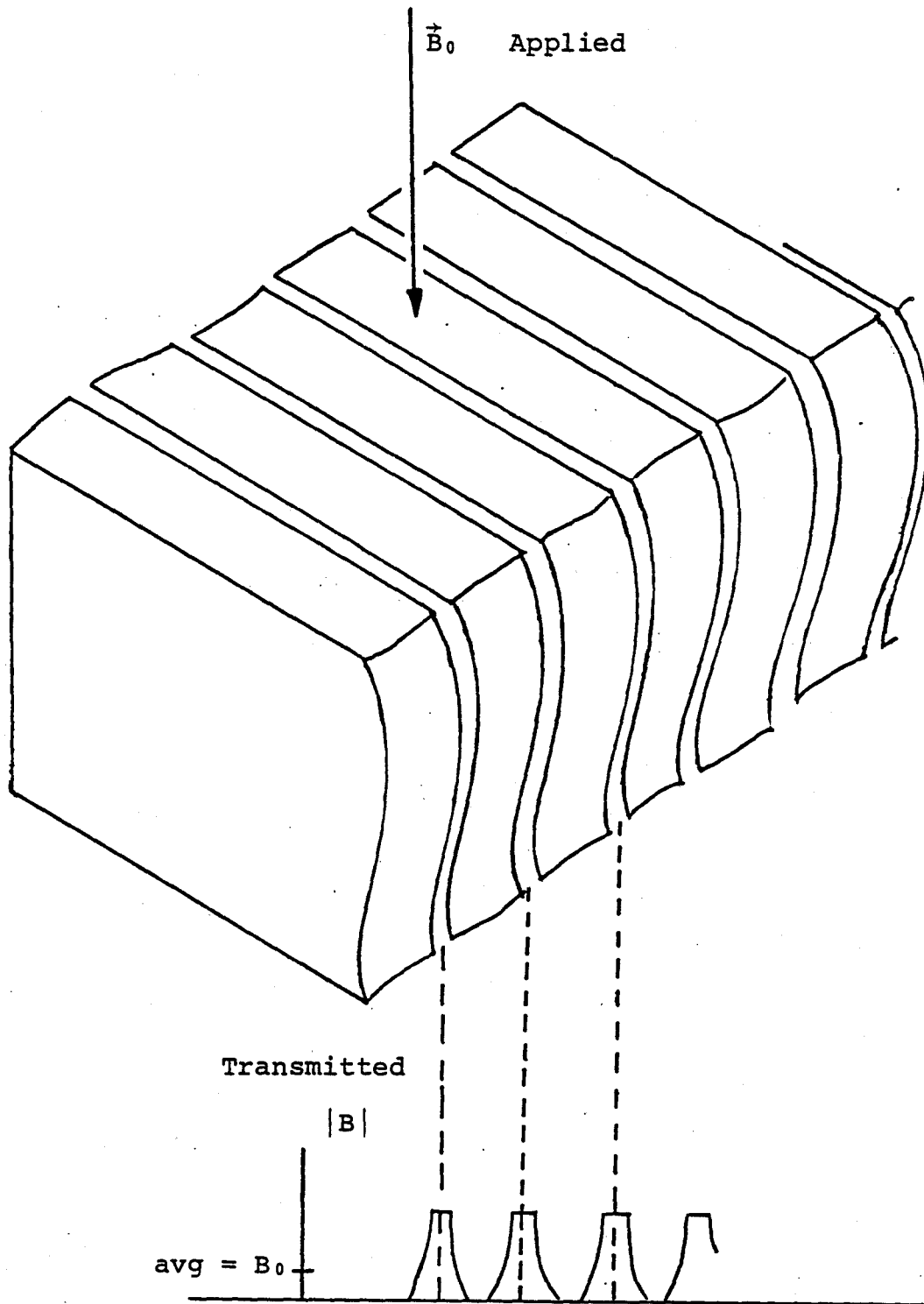


Figure A.II.2. Field penetration, case 1. A vertical field is applied perpendicular to the ends of infinitely wide plates; by symmetry, or $\nabla \cdot B = 0$, the transmitted field is equal to the applied field.

A.II.1.2 Case 2

Infinitely long parallel plates with field applied parallel to their sides is considered next (see Figure A.II.3). Here, surface currents flow which exclude flux from the inside of the conductors. Again by symmetry, or by line-integrating \bar{B} along either path I or II as shown, it can be seen that the transmitted field II is the same as the applied field I. Each path passes through the center of the plates and encloses the same amount of the surface current, so the the line integral of the magnetic field along each is the same. Thus field is not excluded from the other side of the plates.

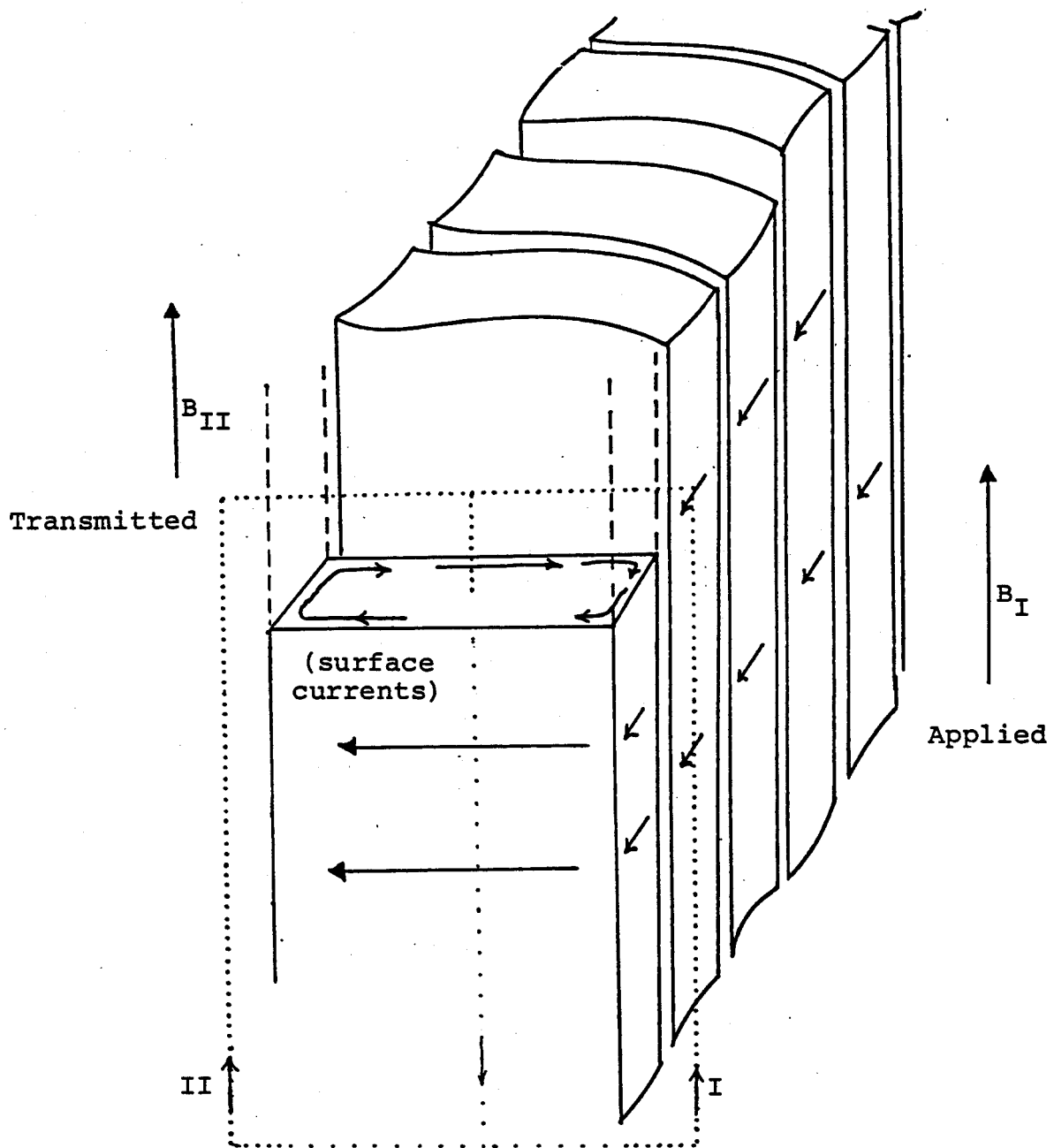


Figure A.II.3. Field penetration, case 2. A vertical field is applied parallel to the sides of infinitely long plates; induced surface currents shield the field from the interiors of each plate, but the field is transmitted past them. Line integrals around path I or II surround the same amount of current, so $B_I = B_{II}$.

A.II.2 Penetration through the Vacuum Chamber Wall

The vacuum chamber is constructed from a stainless steel bellows that is bent into a torus. Several penetration effects occur for a time-varying applied field. For the first, the bellows can be modeled as a straight conducting cylindrical shell in an alternating vertical field. Solution of Maxwell's equations shows that, as the frequency is increased, the field begins to be excluded from the interior at the frequency

$$f = \frac{1}{2\pi\tau} = \frac{1}{2\pi \mu_0 b \sigma \delta}$$

$$= 1.6 \text{ kHz}$$

for the parameters

$$b = \text{radius of shell} = .2 \text{ m}$$

$$\sigma \delta = \text{wall thickness x conductivity}$$

$$= 400 \text{ } \Omega^{-1}$$

or $\tau = .1 \text{ ms}$. Because of the variations in wall thickness around the torus, $(\sigma \delta)$ has been adjusted to its "average" value, i.e., that which gives the measured resistance of the bellows.

The second effect is due to the bellows being formed into a torus; it is a conducting ring with inductance $L = 1.1 \mu\text{H}$ [6] and resistance $R = 8 \text{ m}\Omega$. As such it begins to exclude flux at the frequency

$$f = \frac{1}{2\pi} \frac{R}{L} = 1160 \text{ Hz}$$

or $\tau = .14 \text{ ms}$.

A.II.3 Machine Penetration-Time Measurements

By the use of pickup coils sensitive to poloidal field ($\cos \theta$ coil) and to radial field (saddle coil) just outside the vacuum chamber wall, it is possible to measure these field penetration effects. The pickup coils are described in detail in Chapter 3. The frequency response was found by measuring the signals at the pickup loops when known alternating currents were passed through the the vertical or horizontal field coils.

A graph of pickup signal amplitudes vs. frequency for applied horizontal field is shown in Figure A.II.4. The geometry of parallel plates is basically the same as for an applied vertical field, but the bellows' conducting-ring effect is absent. When the field is excluded from the vacuum chamber, the theta component outside the bellows begins to increase while the radial component decreases, and these changes are clearly shown. Described in section b of this appendix, this is the effect modeled by a long straight cylindrical shell in a transverse field, and occurs at about 2 kHz, close to the predicted value.

The frequency response to applied vertical field is shown in Figure A.II.5. The same long-cylinder effect is apparent, but the effect due to the bellows being a conducting-ring modifies the response. A dip occurs in the B_θ curve as the bellows current rises and flux is excluded from the torus center; this is at approximately 1 kHz, which is again close to the predicted value.

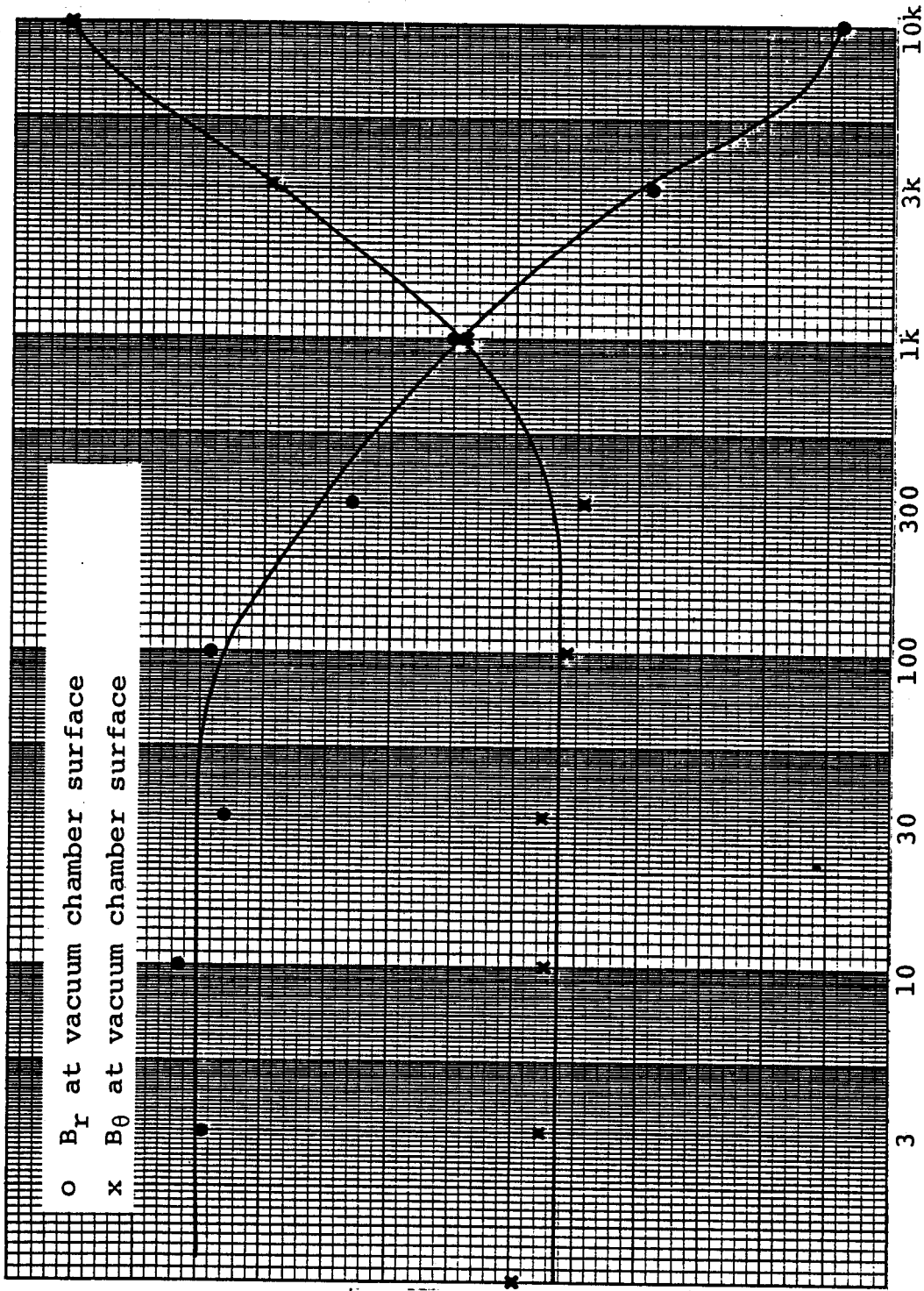


Figure A.II.4. Detected radial and poloidal field at the vacuum chamber surface for an applied horizontal field. As field is excluded from the interior, B_θ begins to rise, while B_r decreases. There is no "conducting ring" effect as for applied vertical field.

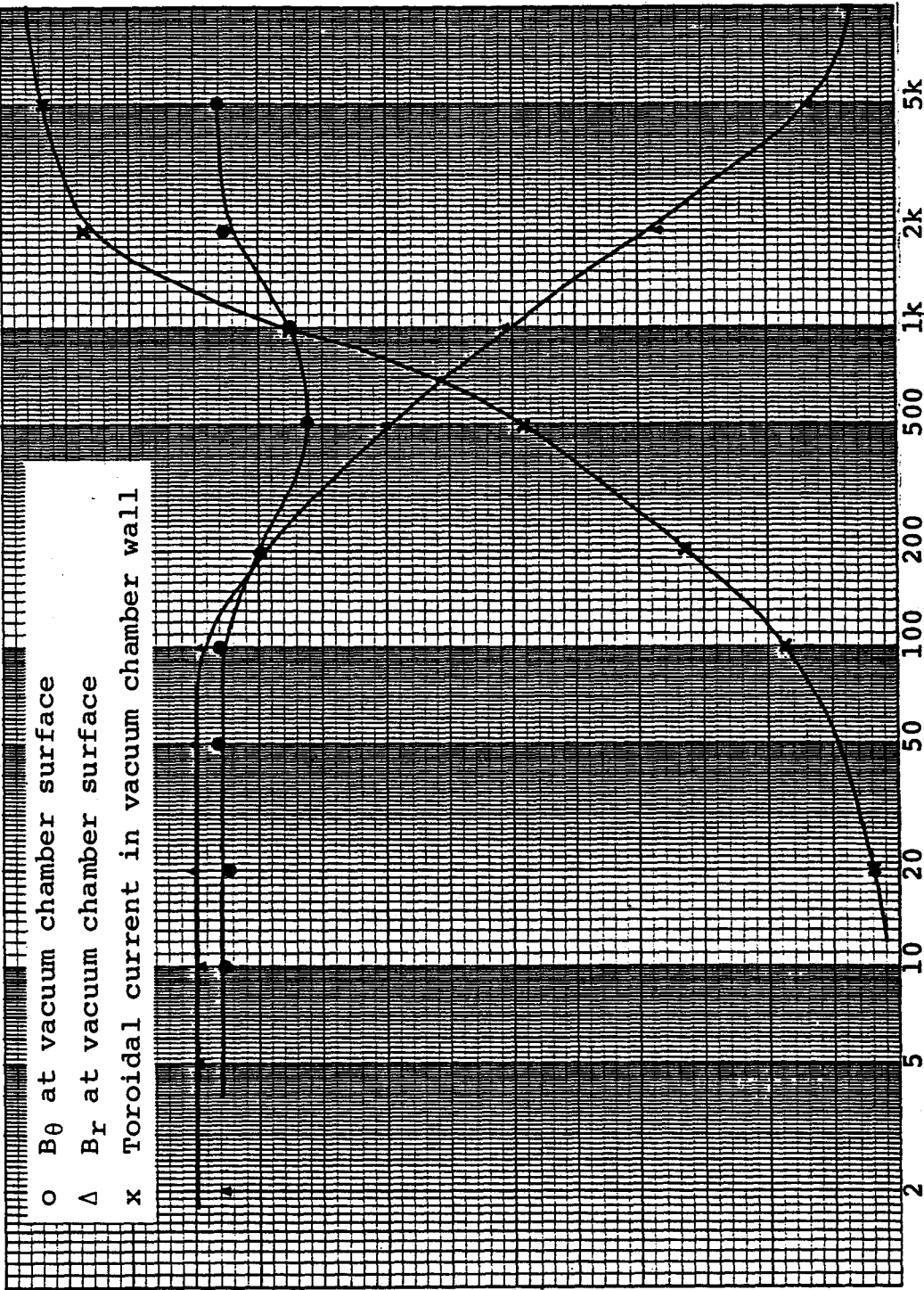


Figure A.II.5. Detected radial and poloidal fields at the vacuum chamber surface for an applied vertical field. Induced bellows current is also shown, and illustrates the onset of the "conducting ring" effect. At a higher frequency, the flux is also excluded from the interior of the vacuum chamber, due to the "long cylinder" effect, causing the $\cos \theta$ signal to remain relatively constant over these frequencies.

In both situations, no real decrease of signal is observed, supporting the earlier argument that the vertical field completely penetrates the toroidal Bitter plates for the frequencies of interest.

Appendix III. Magnetic Field Strengths in Alcator C

Table A.III.1 Midplane Values of the Fields and their Indexes.
 (Note: The total index of two fields B_1 and B_2 is given by:

$$I_{\text{tot}} = \frac{B_1 I_1 + B_2 I_2}{B_1 + B_2} .)$$

Table III.1a EF1 Vertical Field at Midplane, for 1 kA

Radius (cm)	Magnetic Field (Gauss)	Index
44	502.	0.16
45	500.	0.18
46	499.	0.19
47	498.	0.21
48	496.	0.23
49	494.	0.25
50	493.	0.27
51	490.	0.29
52	488.	0.32
53	486.	0.35
54	483.	0.37
55	480.	0.41
56	477.	0.44
57	474.	0.47
58	470.	0.51
59	466.	0.55
60	462.	0.60
61	458.	0.64
62	454.	0.69
63	449.	0.75
64	444.	0.80
65	439.	0.86
66	433.	0.93
67	427.	0.99
68	421.	1.06
69	415.	1.14
70	408.	1.22
71	402.	1.31
72	394.	1.40
73	387.	1.49
74	380.	1.59
75	372.	1.70
76	364.	1.81
77	355.	1.93
78	347.	2.06
79	338.	2.19
80	329.	2.33
81	320.	2.47
82	310.	2.63
83	301.	2.79
84	291.	2.96

Table A.III.1b EF2 Vertical Field at Midplane, for 1 kA.

Radius (cm)	Magnetic Field (Gauss)	Index
44	467.	-0.06
45	468.	-0.06
46	469.	-0.06
47	470.	-0.06
48	472.	-0.05
49	473.	-0.05
50	474.	-0.05
51	475.	-0.05
52	476.	-0.05
53	476.	-0.04
54	477.	-0.04
55	478.	-0.03
56	479.	-0.03
57	479.	-0.02
58	480.	-0.02
59	480.	-0.01
60	481.	0.00
61	481.	0.01
62	481.	0.02
63	481.	0.04
64	481.	0.05
65	481.	0.07
66	481.	0.08
67	480.	0.10
68	480.	0.12
69	479.	0.15
70	478.	0.17
71	477.	0.20
72	476.	0.23
73	475.	0.27
74	473.	0.30
75	471.	0.34
76	469.	0.39
77	467.	0.44
78	464.	0.49
79	461.	0.54
80	458.	0.61
81	455.	0.67
82	451.	0.74
83	447.	0.82
84	442.	0.91

Table A.III.1c DF1 Bias Field at Midplane, for 1 kA.

Radius (cm)	Magnetic Field (Gauss)	Index
44	-134.	2.04
45	-129.	2.14
46	-123.	2.24
47	-118.	2.35
48	-113.	2.47
49	-108.	2.58
50	-103.	2.70
51	-98.	2.83
52	-93.	2.95
53	-88.	3.09
54	-84.	3.23
55	-79.	3.37
56	-75.	3.52
57	-71.	3.67
58	-67.	3.83
59	-63.	4.00
60	-59.	4.18
61	-55.	4.36
62	-52.	4.56
63	-48.	4.77
64	-45.	4.99
65	-42.	5.22
66	-39.	5.47
67	-36.	5.75
68	-33.	6.04
69	-31.	6.35
70	-28.	6.70
71	-26.	7.09
72	-24.	7.51
73	-21.	7.99
74	-19.	8.52
75	-17.	9.14
76	-16.	9.86
77	-14.	10.70
78	-12.	11.70
79	-11.	12.93
80	-9.	14.47
81	-8.	16.45
82	-6.	19.13
83	-5.	22.94
84	-4.	28.82

Table A.III.1d DF2 Bias Field at Midplane, for 1 kA.

Radius (cm)	Magnetic Field (Gauss)	Index
44	153.	0.03
45	154.	0.03
46	154.	0.04
47	154.	0.04
48	154.	0.05
49	154.	0.06
50	154.	0.06
51	154.	0.07
52	154.	0.08
53	154.	0.09
54	154.	0.10
55	153.	0.11
56	153.	0.13
57	153.	0.14
58	153.	0.16
59	152.	0.17
60	152.	0.19
61	152.	0.21
62	151.	0.23
63	151.	0.25
64	150.	0.28
65	150.	0.30
66	149.	0.33
67	149.	0.36
68	148.	0.39
69	147.	0.42
70	146.	0.46
71	145.	0.50
72	144.	0.54
73	143.	0.58
74	142.	0.63
75	141.	0.68
76	140.	0.74
77	139.	0.79
78	137.	0.85
79	136.	0.92
80	134.	0.99
81	133.	1.06
82	131.	1.14
83	129.	1.22
84	127.	1.31

Table A.III.1e. Horizontal Bias Field at Midplane, for 1 kA.

Radius (cm)	Magnetic Field (Gauss)	Index
44	41.	
45	42.	
46	43.	
47	45.	
48	46.	
49	47.	
50	48.	
51	50.	
52	51.	
53	53.	
54	54.	
55	55.	
56	57.	
57	58.	
58	60.	
59	61.	
60	63.	
61	64.	
62	66.	
63	68.	
64	69.	
65	71.	
66	72.	
67	74.	
68	76.	
69	78.	
70	79.	
71	81.	
72	83.	
73	85.	
74	87.	
75	89.	
76	91.	
77	92.	
78	94.	
79	96.	
80	98.	
81	100.	
82	102.	
83	104.	
84	106.	

Table A.III.1f Stray Toroidal Field at Midplane, for 100 kA
 Entries are for a single turn current modelled as a Gaussian 25 cm wide, centered at the midplane. (These values are good approximations for Gaussians centered within 5 cm of the midplane.)

Radius (cm)	Magnetic Field (Gauss)	Index
44	-	
45	-	
46	-	
47	-	
48	-	
49	-	
50	-247.	0.89
51	-241.	1.04
52	-234.	1.17
53	-227.	1.29
54	-219.	1.40
55	-212.	1.49
56	-205.	1.58
57	-198.	1.66
58	-191.	1.73
59	-184.	1.80
60	-177.	1.86
61	-170.	1.92
62	-164.	1.98
63	-158.	2.03
64	-152.	2.08
65	-146.	2.13
66	-141.	2.17
67	-136.	2.21
68	-131.	2.25
69	-126.	2.28
70	-121.	2.32
71	-117.	2.35
72	-112.	2.38
73	-108.	2.40
74	-104.	2.43
75	-100.	2.45
76	-97.	2.47
77	-93.	2.49
78	-90.	2.51
79	-87.	2.53
80	-84.	2.55
81	-81.	2.56
82	-78.	2.58
83	-75.	2.59
84	-73.	2.61

e. Horizontal Bias Field at Midplane, for 1 kA.

t in

Radius (cm)	Magnetic Field (Gauss)	Index
44	41.	
45	42.	
46	43.	
47	45.	
48	46.	
49	47.	
50	48.	
51	50.	
52	51.	
53	53.	
54	54.	
55	55.	
56	57.	
57	58.	
58	60.	
59	61.	
60	63.	
61	64.	
62	66.	
63	68.	
64	69.	
65	71.	
66	72.	
67	74.	
68	76.	
69	78.	
70	79.	
71	81.	
72	83.	
73	85.	
74	87.	
75	89.	
76	91.	
77	92.	
78	94.	
79	96.	
80	98.	
81	100.	
82	102.	
83	104.	
84	106.	

represents
tained from

.....
Bias Field

ps nθ.
lculated

Gauss

Gauss

Gauss

Gauss

.....
 $\sum B_n \sin n\theta.$

Gauss

.....
urn" that
nd centered
model is
nsions
toroidal
the minor

Gauss

Gauss

Appendix IV. The Feedback Circuit--Description and Schematic

The feedback circuit can be divided into two sections: the integrators, and the summing and lead network. The integrators are the input stage; in the succeeding stage their outputs are summed, and differentiated for the lead. The integrator signals are also monitored. The final output drives the Transrex SCR power supply through an isolation amplifier, which is external to the circuit.

A.IV.1 The Integrators

In order to allow integration of all fields present in the tokamak, a useable integration time of 8 seconds was aimed for, with minimum output drift being a design priority. Because of the environment, differential inputs are necessary. Reset capability was desired, and also auto-zero compensation for any offset current changes that would occur due to temperature changes or aging effects.

The circuit in Figure A.IV.1 meets these criteria acceptably for use in the feedback system. Op-amp U1 is a differential integrator, U2 is the auto-compensation sample/hold, and U3 and U4 are output buffers.

During quiescent operation, the circuit is in the auto-compensate mode of operation. Just before the plasma pulse, this is stopped and integration begun. In general, the output voltage is not zero just before the plasma shot occurs (due to offset voltage and stray pickup from a number

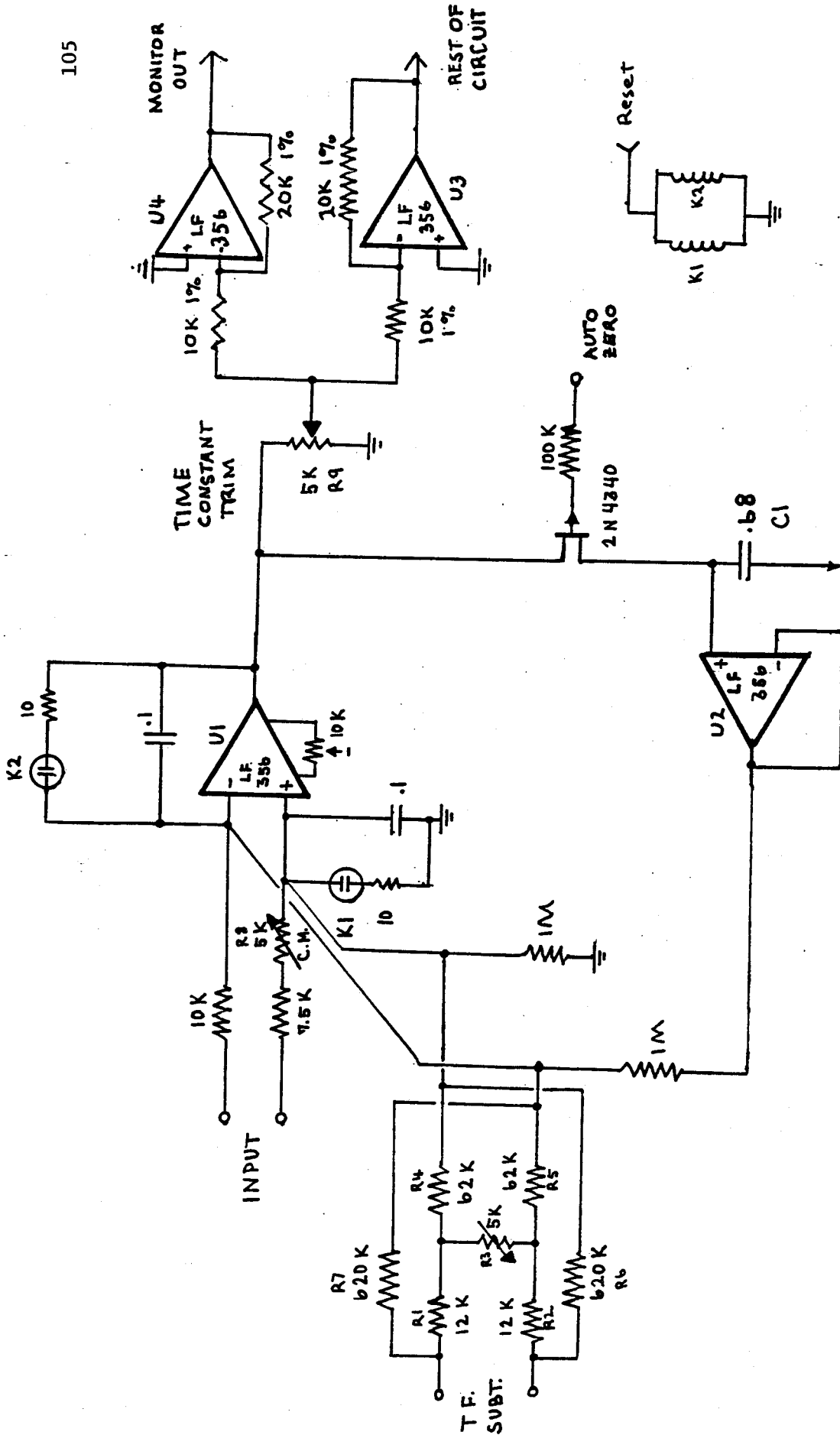


Figure A.IV.1 The Integrator Circuit. The integrator is auto-zeroing, and includes a differential subtraction circuit for stray field compensation. The output goes to the summing and lead circuit, Figure A.IV.2.

of fields), so the relays K1 and K2 are turned on for 30 ms to discharge the capacitors to zero. Integrator reset is accomplished with relays to avoid any unequal leakage currents that might result from use of FET switches.

FET Q1, capacitor C1, and op-amp U2 form a sample and hold for use in the auto-drift compensation. With the FET on, this forms a unity gain follower for DC signals at the output of U1, and op-amps U1 and U2 can be treated simply as a high gain DC amplifier. Unbalanced offset currents generate an output voltage, and this is held by the capacitor during integration (when the FET is off). Drift of the holding capacitor voltage is small and has negligible effect during the 8 seconds of DC-open-loop operation.

Resistors R1 through R7 form an error-field subtraction circuit. This is used to null any signal due to coupling of the toroidal field to the pickup coils. This is a differential subtraction circuit whose contribution may be varied either positive or negative by use of one potentiometer, R3.

In order to minimize common mode sensitivity, the time constants for each side of the integrator may be equalized by adjusting R8. The overall output time constant is adjusted by R9.

Op-amp U3 is a 741, and is used as the monitor output for the integrated signal. Its output is equal to that from U4, which drives the summing and differentiating circuit. The feedback resistors of these two amplifiers are of 1% tolerance, but were matched to be significantly closer.

Two integrator circuits are implemented on a single circuit board. All connections are through a 22 pin edge connector. The component side has a ground plane, and the relays are in dual-inline packages mounted on the board.

The board must be clean, or leakage currents cause output drift. This could probably be avoided by better arrangement of components, with proper low-current shielding techniques applied to the conductor side of the board.

A.IV.2 The Rest of the Circuit

The summing and differentiation circuit is shown in Figure A.IV.2. The outputs from the $\cos \theta$ and saddle integrators are summed with variable weighting. R1 and R2 control the output level from each. Added to them is the output from the plasma current integrator, also variable. Op-amp U10 contributes a differentiated version of the signal, and potentiometer R4 controls the lead time constant. Their sum is the feedback signal, the overall amplitude of which is adjusted by R3. A programming signal is added at this stage, and this becomes the output signal to the power supply. The output is buffered by op-amp U14, and may be clamped to an adjustable level by the circuit around U13. A voltage follower monitors that signal for recording during the plasma shot. All adjustments are on the front panel.

Also shown is the control circuit for the integrators' reset functions. The 555 timers control the length of the integration pulse (U17) and the length of the reset pulse (U16). The firing of the one-shots is externally programmed, or they may be manually triggered.

The inputs to this stage are all monitored by level detectors, U16 and U17. If the integrator outputs are above 12.5 or below -12.5 Volts, a front panel LED indicator is lit to indicate possible saturation.

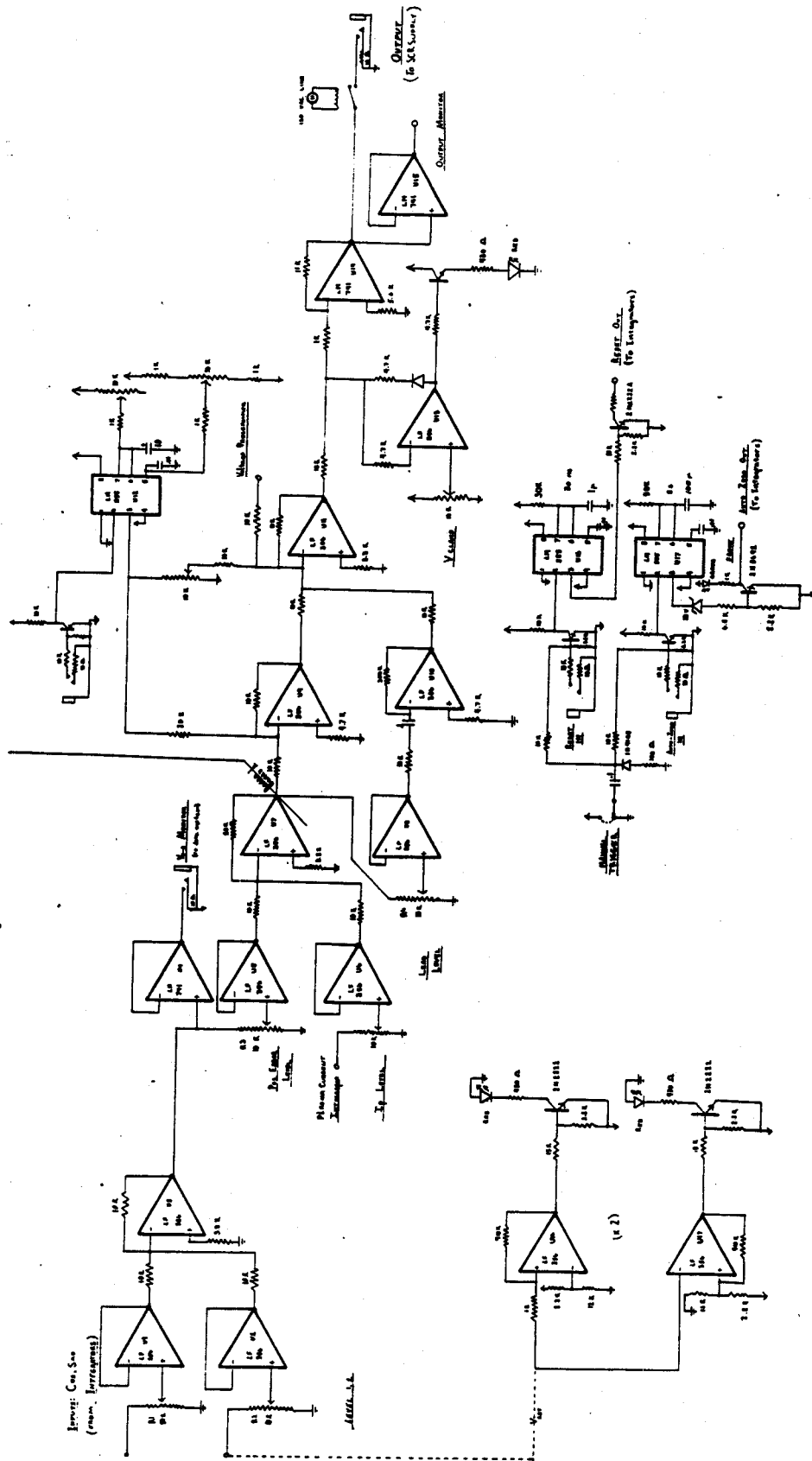


Figure A.IV.2 The Summing and Lead Network. Inputs are the integrated Cosine, Saddle, and I signals. Saturation detectors monitor these signals. The timers for the Integrator reset and auto-zero functions are also shown.

Acknowledgements

I would like to thank Ron Parker for his continuing encouragement and support of my academic work. His guidance in this thesis has been of great assistance; in my career it has been invaluable.

Dave Overskei and Steve Wolfe have always been helpful, both for this work and for my education. I would like to thank them as well as the rest of the Alcatraz group for the help they have given me.

I would also like to thank my friend Susan Byers for her last minute typing and editing.

References

1. Freidberg, J. P. Notes from course 22.615 at MIT. Magnetohydrodynamic Theory. (Fall 1979).
2. Kissel, S. E. Private communication.
3. Wolfe, S. M. Private communication.
4. Shafranov, V. D. Reviews of Plasma Physics Vol. 2, Consultants Bureau, New York (1966) p. 103.
5. Mukhovatov, V. S., and Shafranov, V. D. Nuclear Fusion 11 (1971) p. 605.
6. Malmberg and Rosenbluth. Reviews of Scientific Instruments 36, 12 (1965) p. 1886.
7. Chen, F. F. Introduction to Plasma Physics, Plenum Press, New York (1974) p. 162.
8. Jackson, J. D. Classical Electrodynamics, Wiley, New York (1975) p. 177.
9. Hastings, C. Approximations for Digital Computers, Princeton University Press, Princeton, N. J. (1955) Sheets 48, 49.